NASA Technical Paper 2784

AVSCOM Technical Report 87-B-3

May 1988

Advancing-Side Directivity and Retreating-Side Interactions of Model Rotor Blade-Vortex Interaction Noise

R. M. Martin,
W. R. Splettstoesser,
J. W. Elliott,
and K.-J. Schultz

US ARMY AVIATION SYSTEMS COMMAND
AVIATION R&T ACTIVITY

NASA

NASA Technical Paper 2784

AVSCOM Technical Report 87-B-3

1988

Advancing-Side Directivity and Retreating-Side Interactions of Model Rotor Blade-Vortex Interaction Noise

R. M. Martin
Langley Research Center
Hampton, Virginia

W. R. Splettstoesser
Deutsche Forschungs- und Versuchsanstalt fur Luft- und Raumfahrt
Braunschweig, West Germany

J. W. Elliott
Aerostructures Directorate
USAARTA-AVSCOM
Langley Research Center
Hampton, Virginia

K.-J. Schultz
Deutsche Forschungs- und Versuchsanstalt fur Luft- und Raumfahrt
Braunschweig, West Germany

National Aeronautics and Space Administration

Scientific and Technical Information Division

Abstract

Acoustic data are presented from a 40-percent-scale model of the four-bladed BO-105 helicopter main rotor, tested in a large aeroacoustic wind tunnel. Rotor blade-vortex interaction (BVI) noise data in the low-speed flight range were acquired using a traversing in-flow microphone array. Acoustic results presented are used to assess the acoustic far field of BVI noise, to map the directivity and temporal characteristics of BVI impulsive noise, and to show the existence of retreating-side BVI signals. The characteristics of the acoustic radiation patterns, which can often be strongly focused, are found to be very dependent on rotor operating condition. The acoustic signals exhibit multiple blade-vortex interactions per blade with broad impulsive content at lower speeds, while at higher speeds, they exhibit fewer interactions per blade, with much sharper, higher amplitude acoustic signals. Moderate-amplitude BVI acoustic signals measured under the aft retreating quadrant of the rotor are shown to originate from the retreating side of the rotor.

Introduction

Helicopter blade-vortex interaction (BVI) noise has in recent years become a topic of great interest in the helicopter acoustics research community. When BVI occurs, this noise mechanism dominates the acoustic signal and is in the frequency range considered the most important to human subjective response. The impulsive noise due to BVI is the result of the aerodynamic interaction of a rotor blade with the trailing vortex system generated by preceding blades. The phenomenon is predominantly generated during low-speed descent, because when the rotor is descending, the separation distance between the rolled-up blade tip vortices and the rotor blades is decreasing. Since the interactions are highly dependent on the wake characteristics, the occurrence of this phenomenon is extremely sensitive to the rotor design and the helicopter operating conditions.

Past experimental work on rotor BVI noise has attempted to define rotor operating regimes, parametric effects, directivity, and scalability of the BVI acoustic signal. Notable efforts in this area have included both flight measurements (refs. 1–4) and wind tunnel programs (refs. 5–11). Results from the in-flight and wind tunnel data of references 1, 2, 5, and 6 have indicated the general directivity patterns of the BVI signal. These researchers found that the impulsive acoustic signal propagates generally forward of the advancing side with the maximum radiation approximately 40° down from the rotor plane. However, the results of the wind tunnel tests of references 8 and 9, which simulated the intersection of a tail rotor with a main rotor vortex, indicated a dipole-like radiation pattern for BVI noise, with the minimum radiation near the rotor plane. Furthermore, references 10 and 11 showed the strongest radiation direction to be 90° below the rotor plane, when measured both ahead of the rotor and on the advancing side of the rotor. The large difference in tip speeds between the rotors tested in references 1 to 7 and that of the smaller scale data (refs. 10–11) may be the cause for the difference in directivity characteristics reported. BVI on the retreating side was reported in reference 11, and some evidence of retreating-side BVI was also reported in reference 3. These conflicting results on advancing-side BVI directivity and the paucity of retreating-side BVI noise data indicate that these phenomena have not yet been conclusively defined spatially or as a function of operating parameters.

The primary objectives of the test program reported here were (1) to acquire a comprehensive data base to improve the definition of the directivity patterns of rotor BVI impulsive noise, (2) to investigate more fully retreating-side BVI noise, and (3) to improve knowledge of the locations of BVI noise sources. The test was performed in the open test section of the Duits-Nederlandse Windtunnel (DNW), a large aeroacoustic test facility, utilizing a four-bladed, 40-percent dynamically scaled model of the Messerschmitt-Bölkow-Blohm GmbH BO-105 helicopter main rotor. High quality acoustic data were acquired due to the excellent fluid dynamic and acoustic properties of the DNW. In particular, the tunnel has quite low in-flow background noise and turbulence levels and a sizable anechoic open test section. The importance of low turbulence airflow on rotor acoustic testing is stressed in reference 12, a comparison of acoustic results from a model rotor tested in both the DNW and the French CEPRA-19 tunnel.

An extensive range of in-flow acoustic measurements were acquired in a plane underneath and upstream of the rotor model using a traversing nine-microphone array. A digital acoustic data acquisition system was employed to guide the choice of the test matrix and identify optimum measurement locations by using on-line identification of strong BVI noise test conditions. The BVI directivity was investigated by using a large traversing microphone array. A high quality data base for acoustic localization techniques was acquired through a large range of measurement locations. The occurrence of BVI acoustic signals created on the retreating side of the rotor was pursued by positioning the microphone array under and downstream of the rotor, in positions

previously found to best measure the phenomenon (ref. 11).

Secondary objectives of the program were (1) to assess the far field of rotor BVI noise, (2) to extend the investigation of reference 5 into the scalability of BVI noise from model- to full-scale at high advance ratio, (3) to explore the parametric effects of advance ratio, tip-path-plane angle, and thrust coefficient on BVI noise, and (4) to acquire a data base for future development of a BVI noise prediction methodology.

The experiment was performed jointly with research personnel of the German Aerospace Research Establishment, the Deutsche Forschungs- und Versuchsanstalt fur Luft- und Raumfahrt (DFVLR). The model rotor and the rotor test stand were provided and operated by research personnel of the Rotary Wing Aircraft Branch of the DFVLR Institute of Flight Mechanics. Acoustic instrumentation support was provided by research personnel of the Technical Acoustics Division of the DFVLR Institute of Design Aerodynamics.

The general philosophy and experimental approach of this program are documented in detail in reference 13. This reference fully documents the model test rig, instrumentation, data acquisition and reduction, acoustic calibrations, and experimental procedures, in addition to presenting a large representative set of the averaged acoustic signals. Some initial test results on acoustic directivity and retreating-side BVI have also been presented in reference 14. The results presented here include the following: an investigation of the acoustic far field of the BVI signals, the definition of acoustic radiation patterns of BVI noise in a plane under and upstream of the rotor, observations of the temporal characteristics of the BVI signals at high BVI noise conditions, and illustration of BVI signals originating from the rotor's retreating side.

Symbols

C_T rotor thrust coefficient, $T/\pi\rho\omega R^4$

M_H hover tip Mach number

R rotor radius, 2.0 m

r radial distance from rotor hub to microphone (see fig. 1), m

r_s radial distance from BVI source location to microphone (see fig. 1), m

T rotor thrust, N

V flow speed, m/sec

X_w streamwise location of traversing array relative to hub, positive upstream (see fig. 1), corrected for streamwise movement of hub due to model pitch, m

Y_w cross stream location of traversing array microphones relative to hub, positive on advancing side (see fig. 1), m

Z_w vertical location of traversing array, positive above hub (see fig. 1), m

α_{shaft} angle of rotor shaft from vertical, deg

α_{TPP} rotor tip-path-plane angle, positive nose up (see fig. 1), deg

θ polar angle, angle centered at hub from tip-path plane to microphone location, positive down (see fig. 1), deg

θ_s polar angle, angle centered at BVI source location from tip-path plane to microphone location, positive down (see fig. 1), deg

μ advance ratio, $V/\omega R$

ρ density, kg/m^3

ψ azimuth angle in the tip-path plane from rotor hub to microphone location, zero over tail, 90° over rotor advancing side (see fig. 1), deg

ψ_s azimuth angle in the tip-path plane from BVI source location to microphone location, zero over tail, 90° over advancing side (see fig. 1), deg

ω rotational speed of rotor, cycles/sec

Abbreviations:

BVI blade-vortex interaction

DFVLR Deutsche Forschungs- und Versuchsanstalt fur Luft- und Raumfahrt

DNW Duits-Nederlandse Windtunnel (German-Dutch Wind Tunnel)

Mic microphone

PaN unit of normalized acoustic pressure in pascals (divided by $2R/r_s$)

rms root-mean-square

rpm revolutions per minute

Experimental Apparatus

Wind Tunnel

The test was performed in the open test section of the Duits-Nederlandse Windtunnel (DNW), located

in the North East Polder, The Netherlands. The DNW is a subsonic, atmospheric, closed circuit wind tunnel with three interchangeable, closed test section configurations and one open configuration. The open configuration employs an 8×6 m contraction section and a 19-m-long test section surrounded by a large anechoic hall of about 30 000 m^3 lined with absorptive acoustic wedges. The tunnel has very good fluid dynamic qualities when operated in the open throat mode (refs. 15–18). A potential core of uniform flow (mean flow velocity of $\pm 0.5\%$) has been defined as a 5×3 m core within the 8×6 m nominal test section at 7 m from the jet exit. Turbulence intensities in both the streamwise and the cross stream direction are less than 0.5 at this location.

Model Rotor Test Apparatus

Model Test Stand and Support

The DFVLR rotor test stand (refs. 19–21) is shown installed in the DNW open test section in figures 2 and 3. Details of the rotor test stand are given in table I. The stand consists of three major subsystems: the hydraulic drive system, the rotor balance system, and the rotor control system.

The rotor balance system is a six-component balance containing separate measuring elements for static and dynamic load components. The rotor control system is a swashplate system consisting of three electric actuators which provide collective and cyclic blade pitch control. A potentiometer at the root of one of the blades measures the blade angle of incidence during rotation.

During this test, the rotor test stand was housed within an acoustically insulated fiberglass shell and was attached to the computer-controlled, hydraulic sting support mechanism. The sting was covered with a streamlined sound absorptive lining to minimize acoustic reflections. The sting control system was programmed to keep a model reference point at a preselected height in the test section, for the range of angle of attack (α_{shaft}). However, it was not possible to maintain the reference point at a fixed streamwise location for the range of angle of attack.

Model Rotor

The rotor is a 40-percent, dynamically scaled model of a four-bladed, hingeless BO-105 main rotor (fig. 4). The rotor has a diameter of 4 m with a root cutout of 0.350 m and a chord length of 0.121 m. The rotor blade is constructed of an NACA 23012 airfoil, with the trailing edge modified to form a 5-mm-long tab, to match the geometry of the full-scale rotor. The rotor blades have $-8°$ of linear twist, a standard square tip, and a solidity of 0.077. Further details are given in table I and reference 19. The rotor blades are made of glass-fiber-reinforced plastic and have essentially the same mass and stiffness distributions as the full-scale rotor. However, the blade chord length ($0.061R$) is a slightly larger scale than the full-scale rotor chord ($0.054R$) in order to maintain the proper Locke number scaling (ratio between the aerodynamic forces and the mass and elastic forces, ref. 19). Each blade is equipped with a small tab located at 70 percent of the radius, measuring 60×10 mm (shown in fig. 4). These tabs, in addition to the pitch rods, are used to adjust the track of each blade in the rotor system. Strain gages installed near the root of each blade are used to measure the blade flapping, lagging, and torsional moments. The nominal rotor operating speed was 1040 rpm, giving an acoustic blade-passage frequency of about 70 Hz. The nominal hover tip Mach number was 0.64.

Rotor Performance Data Acquisition and Reduction

The rotor performance data were obtained from the rotating and fixed systems of the DFVLR test stand control system (ref. 20). The rotating system acquired the signals of the strain gages on the rotor blades (flapping, lagging, and torsional moments), on the control rods (pitch link forces), on the rotor shaft (bending moment), and on the blade root potentiometer (blade pitch angle). The rotating signals were transmitted by two 16-channel pulse-code-modulated encoders on the rotating rotor head, multiplexed, converted to a digital form, transmitted through slip rings, converted back to analog form, and then merged with the fixed system data. The fixed system signals were acquired from the displacement transducers, the static and dynamic balance transducers, the shaft torque transducer, the shaft rpm encoder (360-per-revolution), and the shaft position encoders (once-per-revolution and 512-per-revolution).

Details of the rotor data processing are given in reference 21 and are summarized here. For all signals, 20 revolutions of time domain data were written to digital tape. For on-line analysis and control the central processor performed a Fourier analysis of the data of a single revolution. A second processor provided continuous on-line display of the rotor control parameters: hover tip Mach number, thrust, hub moments, blade bending, and pitch link loads. The final processing of the rotor performance data was done off-line by averaging the results of the 20 revolutions of stored data.

Matrix of Test Conditions

A nominal test plan was developed to investigate the three primary objectives and concentrated on two thrust coefficients, 0.0044 and 0.0030, and the forward speed range of 20 to 40 m/sec ($\mu = 0.09$ to 0.18) at a range of tip-path-plane angle for constant nominal hover tip Mach number of 0.64. The value of 0.0044 is the nominal thrust coefficient for the full-scale BO-105, while the value of 0.0030 was chosen as a reasonable lower limit of thrust level. To investigate the secondary test objectives, a smaller set of conditions included velocities of 50 and 60 m/sec, thrust coefficients ranging from 0.0036 to 0.0056, and hover tip Mach numbers ranging from 0.56 to 0.72.

To determine the optimum test conditions for strong BVI noise generation and the optimum measurement locations for the traversing microphone array, an exploratory approach was used. To minimize testing time during this exploratory phase, acoustic data were acquired with an on-line digital system and were not recorded on analog tape. The on-line analysis performed during this exploratory matrix was used to fine-tune the final, more extensive, test matrix, for which acoustic data were recorded on analog tape for postprocessing. The initial exploratory matrix is described in table II, and the final expanded test matrix in table III. Most of the data presented here are from the on-line analysis of the exploratory matrix. A large representative set of the postprocessed acoustic signals from the final test matrix are presented in reference 13.

Acoustic Instrumentation

The acoustic instrumentation consisted of a nine-microphone in-flow array mounted on a traversing system and two in-flow microphones mounted on the rotor fuselage as shown in figures 2 and 3. The microphones were ½-in. pressure-type condenser microphones equipped with standard "bullet" nose cones. Each complete microphone system (microphone, preamplifier, and adapter) was calibrated using the electrostatic actuator method to document its frequency response. This response was flat between 5 and 5000 Hz, sufficient for the frequency range of the BVI noise (approximately 500 to 3000 Hz for model scale).

Signal conditioning of the microphones was performed by computer-controlled amplifier and filter systems. The amplitude and phase characteristics of the two-pole Butterworth filters were investigated before the test for high-pass filtering at three nominal cutoff frequencies. The amplitude response is flat in the passband. The phase shift is 180° at the cutoff frequency f_c, is approximately 40° at $5f_c$, and negligible at approximately $10f_c$. The filters were found to be well matched in their phase characteristics, within 1° in the passband.

To verify the frequency response of the entire measurement system in situ (from preamplifier to tape recorder), a white noise signal was inserted simultaneously into each preamplifier and recorded on tape. The auto and cross power spectral densities of the white noise signal were checked to ensure flat frequency response and to document phase lag between channels.

The digital amplifier and filter settings were transmitted to a second, larger computer. During testing, up to 10 microphone channels could be digitized using a 12-bit, high-speed simultaneous analog-to-digital converter. The computer was employed to control the analog-to-digital converter, to store calibration and amplification factors, and to perform on-line time domain and spectral analysis. A two-channel fast Fourier transform analyzer was also employed for quick-look analysis during testing.

Microphone calibrations were performed using a sound level calibrator at the beginning and end of the test. All microphone gains were adjusted to produce 500-mV rms output for an acoustic level of 114 dB at 1000 Hz. In addition, a daily calibration of a 1000-Hz, 500-mV rms signal was recorded on all channels by signal insertion at the tape recorder inputs.

Microphone Array Traverse System and Fuselage Microphones

The microphone array traverse system consisted of a horizontal wing with its span normal to the flow direction and a traverse system with a total range in the flow direction of 8.2 m (7 m upstream, 1.2 m downstream of the hub, see fig. 3). The microphones were arranged symmetrically with respect to the tunnel centerline, spaced 540 mm apart. The array vertical position was nominally 2.1 m below the rotor hub, although a small set of data was acquired at 1.6 and 2.6 m below the hub. The microphone holders employed a "soft" vibration-isolating mounting. The total height of the entire structure was such that only the streamlined wing support struts crossed through the shear layer. The wing and support struts were covered with an open-cell foam airfoil section. The supporting structure was covered with a 0.1-m-thick foam lining except at the base, which was covered with 0.8-m foam wedges.

The traverse mechanism was powered by a variable-speed dc electrical motor. Control and positioning was obtained with a servo position controller. The positioning accuracy was 2 mm. Prior to data acquisition, the alignment of the traversing array was

calibrated over its range of motion. The alignment in the cross flow direction was ±2 mm; in the vertical direction, less than ±1 mm. The deflection of the traversing array due to aerodynamic drag was on the order of 9 mm in the streamwise direction at 60 m/sec. The accuracy of this correction is estimated to be ±3 mm. These deflections were calculated off-line and applied to the measured array position data to correct the calculated microphone positions.

Two microphones were also mounted on the fuselage, one under each side of the rotor disk, at azimuth angles of approximately 90° and 270°. These microphones were mounted in vibration isolation mounts similar to the mounts for the traversing array microphones. Data from these locations are not presented here but are discussed in reference 13.

Acoustic Data Reduction and Analysis

The 10-channel analog-to-digital conversion system described in the section entitled "Acoustic Instrumentation" was employed for on-line processing of the acoustic data. The on-line results were primarily used during the exploratory stages of the testing to verify data quality and assist in fine-tuning the final expanded test matrix of BVI test conditions. During the exploratory testing, a high-pass filter at 448 Hz was employed to obtain a better measure of the mid-frequency impulsive content of the signal. This filter removed the first six rotor harmonics so that amplitudes in the time domain would not be biased by the rotor's lowest frequencies, which typically have the highest levels. (For acquisition of the final expanded matrix, a 4-Hz high-pass filter was employed.) After amplification, the data were simultaneously digitized at 20 000 samples per second, with antialiasing filters set at 7 kHz, and calibrated to absolute amplitudes. Thus the frequency range of this analysis was 448 to 7000 Hz, the range where model-scale BVI impulsive noise dominates the spectrum. Ten rotor revolutions of real-time acoustic data and limited narrow-band analyses were stored on computer disk.

Several noise metrics were calculated from these on-line results, the most useful of which was an averaged peak-to-peak value of the filtered signal. The peak-to-peak acoustic pressure for each blade passage (one-fourth of a rotor revolution) in the 10 rotor revolutions was calculated and then averaged to obtain a 40-average metric of the mid-frequency impulsive content of the signal. This metric is a useful estimate of the BVI impulsive content, as it does not contain the low-frequency loading or thickness noise harmonics.

Data Quality

The following topics regarding the quality of the data were investigated: tunnel flow quality, rotor performance data, background noise, acoustic reflections, and the steadiness and repeatability of the rotor acoustic data. These topics are discussed in detail in reference 13 and are only summarized here.

In the low-speed range, the open-jet tunnel configuration can exhibit a low-frequency, low-amplitude pulsation of the mean flow, similar to pulsations previously observed in other open-jet tunnels (ref. 22). In some cases this pulsation caused problems in achieving stable rotor performance parameters, so that some parts of the test matrix had to be redesigned or omitted. Overall, this pulsation was of sufficiently low frequency to be considered quasi-steady compared with the analysis time for both the rotor performance and the acoustic data.

Background noise data were acquired with all testing and model hardware installed in the tunnel. The blades were not installed, but the hub was spinning at nominal speed (1040 rpm). The effect of tunnel speed on the background noise was measured for a range of tunnel speeds at a fixed nominal traverse position (3 m upstream of the hub). Each of the nine microphones located on the traversing array show generally the same background noise levels at this position. The background noise levels measured by the fuselage microphones are higher at the lower tunnel speeds, but are roughly the same at the higher speeds as those measured by the traversing microphones. The higher frequency noise levels for all microphones begin at about 35 dB at 20 m/sec and increase to about 55 dB at 60 m/sec.

The effect of traversing array position on background noise was also investigated. The spectral levels of the traversing microphones increase consistently (by about 10 dB) as the traverse moves downwind and closer to the model. This increase in level at downstream positions is probably due to the increased proximity of the microphones to the bottom shear layer (see fig. 3(b)) and due to the increased proximity to the model system. The levels measured at the fuselage microphones appear to be fairly insensitive to the traverse position, indicating that the traverse itself is not creating additional background noise.

Discrete tones were measured by some of the traverse microphones, particularly at tunnel speeds

of 30, 40, and 50 m/sec, in the range of 2 to 5 kHz. The tone frequencies are not related to tunnel speed. The highest levels of these tones appear to be about 70 dB, which is typically much lower than the rotor signals in that frequency range.

From the above results, the highest background noise for the traverse microphones occurs when the traverse is farthest downstream, at the highest tunnel speed. The highest background noise for the fuselage-mounted microphones probably occurs at the largest shaft angle and highest tunnel speed. Several test conditions fitting these conditions were chosen and the rotor signals were compared with the background noise. The rotor spectra and the background spectra are almost identical at the first spectral line (20 Hz), but above this point the rotor spectrum is at least 5 dB higher than the background spectrum and typically 20 dB higher in the frequency range dominated by BVI noise. The results indicate that the background noise levels are not a contaminant for any of the microphone measurements.

To measure the potential contamination of the rotor signal due to reflections, small explosive charges were specially mounted on the model rotor test rig and detonated to create an impulsive noise source. Approximately 30 charges were ignited to assess the acoustic reflections for several traversing array positions and both with and without tunnel flow. For all the tested configurations, the reflected signals were typically less than 10 percent of the direct blast signal, or at least 20 dB down from the direct signal, and in many cases were of negligible amplitude. The effect of increasing tunnel speed was found to be negligible, as was the effect of rotor hub vertical position.

Acoustic diffraction for the traversing array microphones was identified and is due to the presence of the fuselage. When the traversing array is moved close to the model, the microphones at one end of the traverse are shielded from the acoustic signal from the opposite side of the rotor disk. This was quantified by comparing the known propagation distances (from the source to each microphone) with the measured blast signal arrival times, amplitudes, and model geometry. For traverse positions that are close to and under the model, the blast signals received by the "shielded" microphones are not the direct signal but a combination of a reflected and a diffracted signal, with significantly lower amplitudes. These results indicate that the directivity or absolute levels of advancing- or retreating-side BVI cannot be accurately determined from the shielded microphone locations. The conclusions can be summarized in the subsequent table.

Source azimuth, ψ_s, deg	X_w, m	Shielded microphones
60	2.0	1, 2, 3, 10
	1.0	1, 2, 3, 4, 10
	−.7	1, 2, 3, 4, 10
300	2.0	7, 8, 9, 11
	1.0	6, 7, 8, 9, 11
	−.7	6, 7, 8, 9, 11

The steadiness and repeatability of the rotor acoustic signal were studied for several test conditions repeated during the experiment. A comparison of instantaneous and averaged time histories showed that the general features of the instantaneous data are consistently seen in the averaged waveform. The repeatability of a specified rotor condition at different times during the test program was also verified.

Testing Procedures and Measurement Accuracy

Corrections to the free-stream flow angle and speed due to the presence of the lifting rotor in the test section were calculated according to the method of Heyson (ref. 23) and applied to the measured data off-line to obtain the corrected tip-path-plane angles presented here. These corrections are considered reasonable estimates of the true flow angle at moderate tunnel speeds, but become less reliable as the correction increases at the lower tunnel speeds, less than 20 m/sec.

Because of the pivoting of the support sting to achieve a specified shaft angle, the center of the rotor hub experiences both a vertical and a streamwise translation. The sting controller was programmed to reposition the hub at the same vertical position for any shaft angle. The streamwise movement of the rotor hub could not be corrected by repositioning the sting, but is calculated off-line and is accounted for in the calculation of microphone locations. The streamwise position of the microphones X_w is thus corrected for the movement of the hub due to model pitch angle.

In addition to the kinematic motion of the sting support, the actual rotor hub position was also influenced by vertical deflections due to its weight, the rotor angle, the rotor thrust level, and aerodynamic drag. These effects were calibrated in hover before data acquisition by measuring the rotor hub position for the ranges of shaft angle, rotor thrust, and tunnel speed contained in the test matrix. These corrections were then applied to the data off-line. The accuracy of the rotor hub position measurements is ±2 mm.

The rotor parameters—tip-path-plane angle, hover tip Mach number, and thrust—were set using the digital displays at the rotor controls. The rotor operator set the rotor speed for the desired value of hover tip Mach number, simultaneously adjusting collective pitch to obtain the desired thrust. The rotor was operated so that the first harmonics of the shaft bending moments and of lateral and longitudinal flapping were as close to zero as possible. In this case, and neglecting blade bending, the measured rotor shaft angle was thus equivalent to the tip-path-plane angle.

The nominal thrust coefficients tested were 0.0030 and 0.0044. The actual average thrust coefficients were 0.0029 and 0.00435 with standard deviations of 3% and 1.4%, respectively. The nominal hover tip Mach number was 0.64, with an average and standard deviation of 0.636% and 0.5%. The first harmonics of lateral and longitudinal flapping angles were generally less than 0.3°. During the pretest calibrations, a check was made to ensure that a change in the traversing array position in the test section did not affect the rotor performance by requiring changes to the rotor control inputs.

Acoustic Results

Validation of Acoustic Far Field of the BVI Signal

As shown in figure 3(b), the traversing microphone array could acquire measurements over a range of 4.2 m in the cross flow direction, a range of 8.2 m in the streamwise direction, and 1.0 m vertically. This results in a large range of radial distances between the microphones and the BVI noise source. To remove the effect of spherical spreading at each location, the data must be normalized to a reference propagation distance. Such a normalization assumes that the measurements are in the acoustic and geometric far field of the noise source. There is no clear or even commonly accepted definition of the acoustic or geometric far field, particularly for a complex source such as rotor BVI noise, although a distance of one wavelength has been claimed for the acoustic far field and a distance of 3 to 4 times the source dimension has been claimed for the geometric far field (ref. 24). Assuming the model-scale BVI signal to be in the range of 500 to 3000 Hz (ref. 7), at the closest measurement locations the microphones are between 3 and 20 wavelengths from the rotor. Assuming the BVI source's characteristic length to be one rotor chord length, at the closest measurement locations the microphones are about 20 chords from the rotor.

In view of the uncertainty of the far-field assumption, data were acquired to validate the assumption for the data presented here. Acoustic data at a strong BVI test condition were acquired with the traversing array in two horizontal planes below the rotor ($Z_w = -1.6$ and -2.6 m). The streamwise locations of the traverse in these two horizontal planes were set to acquire data on the same acoustic ray originating from a BVI source located on the advancing side. The objective was to ascertain the degree to which the BVI signals follow the spherical spreading decay of the far field. An earlier investigation of this scaling (ref. 14) considered the peak BVI amplitudes. A more in-depth approach considering the BVI spectral levels and time history characteristics is now presented here.

First, an acoustic triangulation technique (ref. 25) was applied to the strongest BVI impulse in the data to estimate its location on the rotor. This location was found to be $r/R = 0.70$ and $\psi = 60°$. The available measurement locations were studied to find sets of two locations on the same acoustic ray from this source (same θ_s and ψ_s, see fig. 1), but in two different horizontal planes (at two different distances). The microphone locations in the two planes were typically within $\pm 2°$ of each other in both θ_s and ψ_s. A metric of the BVI spectral level for each measurement was calculated by summing the energy in the 500- to 3000-Hz band of the averaged narrowband spectra (refer to ref. 13). This band was chosen to remove the low-frequency harmonics, as it is felt that none of the measurement locations are in the acoustic or geometric far field of the low-frequency rotor loading and thickness noise harmonics. This BVI metric was then plotted versus distance from the source for microphones located on the same acoustic rays from the source. The effect of convection on the acoustic paths is small due to the low Mach number and was not considered in this analysis.

Figure 5 presents the BVI spectral metric for a typical descent condition ($\mu = 0.141$, $\alpha_{TPP} = 3°$, $C_T = 0.0044$, $M_H = 0.64$) versus radial distance to the BVI source for several acoustic rays. A sound pressure level decay rate of –5 to –6 dB per doubling of distance was obtained for most of the acoustic rays considered. The average decay rate for all rays is –4.7 dB. If the measurements were in the far field, a –6-dB decay rate per doubling of distance would be observed. If the data contained significant near-field acoustic content (signals which decay with $1/r^2$), the decay rate would be closer to –12 dB per doubling of distance. The fact that the decay rate is not steeper than –6 dB per doubling of distance shows that the far-field normalization of these measured data is a conservative approach.

The acoustic time histories at the two locations on several of these rays were also compared to validate the far-field assumption. The averaged time histories (refer to ref. 13) were digitally filtered with a passband of 500 to 3000 Hz, to yield a time history representative of the band-limited sound pressure level used for figure 5. The signal of the most distant measurement was then scaled with the distance ratio of the two locations and plotted with the closer measurement. If the far-field assumption is valid, this scaling will collapse the data to the same curve. Figure 6 shows the two signals measured along rays 9 and 11 (from fig. 5), which exhibited a −6-dB and −3.5-dB decay, respectively. The signals have been rotated to align the BVI peaks. Figure 6(a) shows very good comparison of the BVI peak shapes and amplitudes, indicating that the far-field scaling is valid. Figure 6(b) also shows a good comparison of the BVI impulse shapes, but for most of the impulses, the most distant measurement, when scaled using the far-field assumption, has slightly higher amplitudes than the nearer measurement, as indicated by the −3.5-dB decay rate from figure 5.

From these results it is concluded that the far-field scaling of the BVI content of the measured acoustic signals is a reasonably valid and in some cases conservative approach to estimating the true far-field signal.

Flight Conditions for "Maximum BVI" Noise

The first phase of the test matrix consisted of exploratory searches to locate the rotor conditions (advance ratio and tip-path-plane angle) for maximum BVI impulsive noise. These exploratory data were acquired for two constant thrust coefficients (0.0044 and 0.0030) and constant hover tip Mach number of 0.64. The data from these exploratory runs were presented in reference 14. The traversing microphone array was set at a nominal position of 4 m upstream of the hub, corresponding to a polar angle (θ) for the array microphones of approximately 25° to 35°. The acoustic data for each condition were high-pass filtered at 448 Hz, the peak-to-peak values calculated, and then normalized to remove the effect of spherical spreading.

It was concluded from these results (ref. 14) that the operating conditions exhibiting the highest impulsive amplitudes and the most directional radiation were measured at $\mu = 0.114$ and α_{TPP} between 2° and 6° and at $\mu = 0.138$ and α_{TPP} between 0° and 4°. The lowest impulsive amplitudes and least directional radiation were found at the lowest and highest advance ratios tested ($\mu = 0.075$, 0.090, 0.160, and 0.183). As a result, several combinations of μ and α_{TPP} exhibiting high BVI noise impulsive levels were chosen for more extensive experimental investigation. Thus, the nominal "maximum BVI" conditions chosen for $C_T = 0.0044$ and for a single fixed traversing array position ($X_w = 4$ m) were

μ	α_{TPP}, deg
0.075	4.4
.090	3.9
.116	3.4
.138	2.3
.146	.5
.170	−1.1

Impulsive Directivity at Maximum BVI Conditions

Once the nominal high BVI test conditions were chosen, the traversing microphone array was employed to define the directivity patterns and to locate the optimum microphone positions for these conditions. For these runs, the traversing array was moved from 6 m upstream of the hub to approximately 1 m downstream of the hub ($X_w = 6$ to −1 m); data were acquired at about every 1 m in a plane 2.1 m below the rotor.

The results of these traversing array data are shown in figure 7 as color contours of the averaged, filtered blade-passage peak-to-peak acoustic amplitudes normalized for spherical spreading. The contours were generated by spline-under-tension, curve-fitting software from 72 independent microphone measurements. To correct for spherical spreading, the acoustic data have been divided by the ratio of a reference distance (4 m, one rotor diameter) to the distance from each microphone to an assumed nominal source location ($r/R = 0.80$, $\psi = 60°$) and are presented as normalized pascals (PaN). Because of the relatively large distances involved, the normalized contour patterns are not particularly sensitive to the exact source location on the advancing aft quadrant ($\psi = 0°$ to 90°) used for the normalization. The error in the normalized acoustic amplitudes due to error in source position in this quadrant is estimated to be ±5% over the measurement plane. The symbol located at $X_w = 0$ m and $Y_w = 0$ m represents the center of the hub, and the large circle of 2-m radius represents the projection of the rotor disk on the horizontal measurement plane.

Figure 7(a) shows the radiation directivity pattern at $\mu = 0.075$ and $\alpha_{TPP} = 4.4°$. The normalized peak-to-peak amplitudes do not vary much over most of the upstream region, although there are three regions of about 30 PaN ahead and upstream of the retreating side ($Y_w < 0$). This indicates that the

impulsive content at this condition is not highly directional and has moderate strength.

The data acquired at higher advance ratios, $\mu = 0.090$, 0.116, and 0.138 (figs. 7(b) to 7(d)), exhibit steadily increasing acoustic amplitudes and clearly show a maximum region under the advancing side ($Y_w > 0$). The maximum region seems to move to the right and downstream as μ increases from 0.090 to 0.138. At $\mu = 0.138$, the highest amplitudes were measured (about 60 PaN), and the maximum location appears to have moved off the measurement plane to the right.

A clearly defined maximum region is still observed at $\mu = 0.146$ (fig. 7(e)), but the peak amplitude has decreased to about 45 PaN. The lowest amplitude and least directionality is seen at $\mu = 0.170$ (fig. 7(f)), with a maximum region of about 25 PaN. The maximum region seems to move back upstream and to the left as μ increases from 0.138 to 0.170. The reader should keep in mind that the tip-path-plane angles for each advance ratio are not the same; rather these data are a collection of the nominal maximum BVI test conditions.

These results clearly show that the directionality of the signal and the direction of strongest radiation are strong functions of the rotor flight condition. The moderate advance ratios, $\mu = 0.116$ and 0.138, exhibit the most directional radiation patterns. An indication of a BVI directivity shift from upstream of the advancing side to upstream of the retreating side can also be seen in the data of reference 26, although this shift was reported to occur with decreasing descent rate (analogous to a decreasing tip-path-plane angle) at constant advance ratio. Unfortunately, it is difficult to correlate this earlier result with the data presented here, as both the advance ratio and the tip-path-plane angle change in the present data.

Temporal Characteristics of Directivity Contours

It is useful to consider the real-time acoustic signals that were used to create the peak-to-peak pressure contour plots. Figure 8(a) presents one representative blade passage of the high-pass-filtered time histories from which the contour plot at $\mu = 0.075$ and $\alpha_{TPP} = 4.4°$ (fig. 7(a)) was derived. The signals are indeed impulsive over the entire measurement plane, except in the shielded region under the retreating side. In general, two to three impulses are seen per blade, and these multiple blade-vortex interactions have approximately the same amplitude. The impulses are the sharpest and strongest at $Y_w = -2$ to 0 m and $X_w = 3$ to 4 m, the same high-level area seen previously on the contour plot.

Figure 8(b) presents the signals for $\mu = 0.090$ and $\alpha_{TPP} = 3.9°$. Again, multiple impulses are seen over most of the measurement plane, but with the sharpest and strongest impulses now seen under the advancing side at $Y_w = 0$ to 1.5 m and $X_w = 1$ to 2 m. At $\mu = 0.116$ and $\alpha_{TPP} = 3.4°$ (fig. 8(c)), the tendency is toward one strong, sharp, positive pressure impulse. Inspection of the data measured at the upstream locations ($X_w = 1$ to 6 m) shows that the strongest impulse gradually changes polarity from upstream of the advancing side ($Y_w = 1.5$ m) to upstream of the retreating side ($Y_w = -1.5$ m), where it becomes a negative impulse. The cause of this polarity change is not known, but may be due to phase changes in the received signal at the nine microphone locations.

At $\mu = 0.138$ and $\alpha_{TPP} = 2.3°$ (fig. 8(d)), the impulses under the advancing side become stronger, but still propagate primarily upstream of the advancing side. The contour plot for this condition (fig. 7(d)) exhibited the highest peak-to-peak pressures and a strong radiation lobe. In general the signals exhibit only one very strong impulse; or if they exhibit more than one impulse, one is much stronger than the others. Some indication of impulsive content is seen at the microphones upstream of the retreating side, but the impulses are less distinct and have lower amplitudes than those in the strong radiation lobe. Some impulsive activity is seen directly under the retreating side, at $Y_w = -2$ to -1.5 m and $X_w = -0.7$ to 0 m. The signals for $\mu = 0.146$ (fig. 8(e)) show essentially the same general results as for $\mu = 0.138$, except with lower amplitudes. Much less impulsive content is seen directly under the retreating side than at $\mu = 0.138$. At $\mu = 0.170$ (fig. 8(f)), the advancing-side interactions appear less distinct and are again lower in amplitude. BVI is again seen under the retreating side.

The temporal characteristics of these six high BVI noise operating conditions lead to several conclusions. The lower speed cases exhibit multiple, equal-amplitude BVI impulses, while the higher speed cases tend to exhibit one single impulse. The lower speed BVI impulses are broader and less sharp and distinct than the moderate-speed impulses. The moderate-speed cases show a more strongly focused radiation, while the lower and higher speed cases exhibit a more omnidirectional pattern.

Retreating-Side BVI

As noted above, considerable impulsive content can be seen in the data of figure 8(d), at $Y_w = -2$ to 0 m and $X_w = -0.7$ and 0 m, directly under the aft retreating quadrant of the rotor. The source of this impulsive activity is not immediately obvious. Recall

that most of this region is blocked by the fuselage from receiving signals from the advancing side of the rotor.

To demonstrate the origins of these signals, figure 9 presents one revolution of all nine acoustic signals measured under the rotor for the six maximum BVI test conditions. The data are in absolute amplitudes, as opposed to the normalized data presented earlier. Two different impulsive signals are identified on these plots. It will be shown that the impulses enclosed by squares were generated on the advancing side, while the impulses enclosed by circles were created by interactions on the retreating side.

The test condition showing the most prominent retreating-side BVI signal is given in figure 9(f) ($\mu = 0.170$, $\alpha_{TPP} = -1.1°$). These data exhibit moderate-level impulsive content at all nine microphones, with the clearest impulses seen in microphones 1, 2, and 3. Acoustic triangulation (ref. 27) was applied using the arrival times of the circled impulses in microphones 1, 2, and 3. The arrows indicate the specific impulses used in the triangulation. The results showed that the signal was indeed generated on the retreating side, although pinpointing the exact source location is difficult with only those three measurement locations. Identification of the retreating-side impulses in the data of microphones 5 through 9 (under the advancing side) is difficult because of the decreasing amplitude of the retreating-side signal. The advancing-side BVI is shown enclosed by the squares at microphones 5 through 9. This advancing-side impulsive content exhibits increased "noisiness" and blade-to-blade differences, particularly at $Y_w = 1$ to 2 m. The retreating-side BVI impulses have almost the same amplitudes as the advancing-side impulses.

Returning to the lower speed cases, figure 9(a) presents all nine microphones at $\mu = 0.075$ and $\alpha_{TPP} = 4.4°$. Microphones 5 through 9 under the advancing quadrant exhibit multiple, low-amplitude BVI signals, enclosed by the squares. Some impulsive content is seen in microphones 1 through 4, but the impulse arrival times are later and later from microphone 4 to microphone 1, indicating that this content is also the advancing-side signal. Figure 9(b) ($\mu = 0.090$, $\alpha_{TPP} = 4.0°$) also shows the advancing-side BVI, but an additional impulsive signal is measured at $Y_w = -2$ to 0 m, shown enclosed by the circles. Both types of impulse are measured at $Y_w = -1$ and −0.5 m. The circled impulses are not distinct enough to apply the triangulation technique. However, the arrival times at microphones 2 and 3 are earlier than those at microphones 1 and 4, indicating that microphones 2 and 3 are the closest to the source, and thus that the source is on the retreating side.

Measurements under the retreating side at $\mu = 0.116$ and 0.138 (figs. 9(c) and 9(d)) show increasingly higher amplitudes for the retreating-side BVI, and both advancing- and retreating-side impulses can be seen in the data at $Y_w = 0$ m. Acoustic triangulation was employed with the circled impulses at these two conditions (see arrows) and again verified that the signals were generated on the retreating side.

At $\mu = 0.146$ (fig. 9(e)) the retreating-side peak-to-peak values begin to decrease. Again, triangulation was used with the circled impulses and confirmed that these signals are retreating-side BVI.

Further data exhibiting retreating-side interactions at lower C_T, 0.0030, are shown for microphones 1 through 4 in figure 10. Impulsive content is clearly seen, with the highest amplitudes at $\mu = 0.184$ (fig. 10(c)).

To compare the amplitudes of the two BVI sources, figure 11 presents the filtered, averaged BVI peak-to-peak acoustic amplitudes expressed in decibels for all the measurements presented in figures 9 and 10. The BVI peak-to-peak level in absolute levels is plotted versus microphone cross stream location (Y_w) for each test condition. Note that the data were not all acquired at precisely the same streamwise location (X_w), but all are under the aft side of the rotor. This figure shows that the BVI impulsive content measured under the advancing side is generally 10 dB higher than that measured under the retreating side, although at $\mu = 0.170$, the two sides have about the same impulsive levels, as shown earlier in figure 9(f).

Although at most of the test conditions the retreating-side signals appear to be weaker than the advancing-side signals, the data presented here do not conclusively define the direction of strongest acoustic radiation for the retreating-side source. Since the advancing-side BVI acoustic signal generally radiates in a direction downward and ahead of the blade leading edge, it is reasonable to assume that the retreating-side BVI signal radiates in an analogous radiation pattern, downwind of the retreating side. Since the measurement locations were limited by practical constraints to only about 1 m downstream of the rotor hub, the data shown here are probably only on the outer edge of the region of strongest retreating-side BVI radiation.

The reader should recall that the data presented in the contour plots of figure 7 are normalized for spherical spreading using the distance to an assumed BVI source on the advancing side. Thus, BVI created on the retreating side is improperly normalized using

a larger distance than the actual distance to the retreating-side source. This incorrectly amplifies the small region of the contour plot where the retreating-side acoustic content dominates, primarily the area around $X_w = -0.7$ m and $Y_w = -2$ to -1 m (see the light blue regions in figs. 7(c) and (d)).

Discussion

The presence of multiple BVI acoustic impulses at the low-speed test condition, $\mu = 0.075$, agrees with existing knowledge of a rotor wake's behavior. At the lower forward speeds, the rotor's wake is convected downstream at a lower speed. In this case the streamwise separation of each tip-vortex filament is smaller; thus the vortices are closer together when viewed from above the rotor. Considering in addition the axial distortion of the tip-vortex filaments which occurs at each side of the rotor (the areas near $\psi = 90°$ and 270°), this wake geometry creates a greater potential for blade-vortex interaction. It has also been shown (ref. 28) that there is a greater potential for the tip vortices to pass above the blades at low advance ratios than at higher advance ratios.

The relatively omnidirectional radiation patterns at the lower speeds may be due to the multiple interactions occurring on the disk at low advance ratio, each having different directivity characteristics. The two-dimensional BVI acoustic theory of reference 29 shows that the primary radiation lobe falls laterally between ±20° of the direction normal to the blade leading edge and longitudinally between 10° and 60° down, indicating that power is radiated strongly forward and downward from the leading edge. Thus, if several interactions occurred, each having its own lobed pattern, at different locations over an azimuth range of 40° to 50°, the resulting acoustic radiation would appear omnidirectional because of several directional patterns being superimposed on each other.

A significant change in the BVI location on the rotor disk may be the reason for the shift in the location of the highest peak-to-peak pressures from ahead of the retreating side at $\mu = 0.075$ to ahead of the advancing side at the higher advance ratios. An intersection occurring between 90° and 120° azimuth would theoretically radiate upstream of the retreating side, while intersections in the aft advancing quadrant would radiate strongly upstream of the advancing side. Thus, as the forward speed increases, the general region of intersections may move aft on the rotor disk, resulting in a shift in the primary radiation region from upstream of the retreating side to upstream of the advancing side. The BVI source location results reported in references 6 and 27 could not identify any obvious trend of source locations with advance ratio; however, reference 30 concluded that at constant advance ratio, the BVI source azimuth tended to increase from the aft advancing quadrant toward 90° azimuth with increasing descent angle (analogous to increasing tip-path-plane angle).

The two-dimensional acoustic theory of reference 29 also indicates that the radiation pattern becomes more directional due to changes in the BVI intersection angle. The BVI intersection angle is the angle (in the disk plane) between the blade leading edge and the projection of the vortex filament. The primary radiation lobe becomes more localized in its polar angle range (angle down from the tip-path plane θ) as the intersection angle changes from parallel to more normal to the blade's leading edge. The acoustic amplitudes theoretically decrease as the intersection angle changes from parallel to normal. The local Mach number also strongly affects the acoustic radiation pattern. As the local Mach number increases, the peak acoustic amplitudes increase quite dramatically and the polar angle θ decreases, moving the primary lobe closer to the rotor plane.

Assuming that all other important parameters (local Mach number, blade-vortex distance, vortex strength) are relatively constant, two-dimensional theory would predict lower acoustic amplitudes for the more directional intersection (more directional acoustic signal). The data presented here show increased acoustic amplitudes for the more focused radiation patterns, but it is extremely difficult to draw any conclusion from these data since the specific intersection geometry and interaction physics were not measured.

Conclusions

Acoustic data are presented for a 40-percent-scale model of the four-bladed BO-105 main rotor, tested in a large aeroacoustic wind tunnel. Rotor blade-vortex interaction (BVI) noise data were acquired in the low- to moderate-speed flight range at constant thrust coefficient and hover tip Mach number to document the rotor's BVI impulsive noise characteristics. A traversing microphone array was employed to map the directivity of BVI impulsive noise from the advancing side and to investigate BVI noise from the retreating side.

The advancing-side BVI directivity data were acquired in a plane below and upstream of the rotor for a set of high BVI noise test conditions with advance ratio μ ranging from 0.075 to 0.170. An investigation into the BVI acoustic amplitude decay with distance for the range of measurement locations was performed to ensure that the measurements were located in the acoustic far field, so that spherical spreading corrections could be employed. The BVI

acoustic radiation patterns can often be strongly localized and are found to be very dependent on the rotor advance ratio and tip-path-plane angle at constant thrust coefficient and hover tip Mach number. The radiation patterns at the lowest advance ratio ($\mu = 0.075$) exhibit a broad directionality in the measurement plane, multiple BVI impulses per blade, the least impulsive interactions, and lower BVI acoustic amplitudes. The radiation patterns at the moderate advance ratios ($\mu = 0.116$ to 0.146) exhibit a highly focused directionality, fewer interactions per blade, sharper impulses, and much higher amplitudes. The region of strongest directionality is generally under and somewhat upstream of the aft advancing quadrant. The radiation patterns at the highest advance ratio ($\mu = 0.170$) exhibited decreased directionality and the lowest BVI amplitudes.

BVI signals of low to moderate amplitude were measured under the retreating side of the rotor. Acoustic triangulation was used to show that these signals were generated on the retreating side of the rotor. This retreating-side BVI generally has levels about 10 dB lower than the signal from the advancing side, although in one case the retreating-side BVI had energy equivalent to the advancing-side signal. A complete documentation of the retreating-side BVI directivity pattern was not possible from the available data due to physical limitations of the measurement hardware. A better assessment of this noise source's directionality and importance relative to advancing-side BVI would require further extensive measurements in the region downstream of the retreating side.

NASA Langley Research Center
Hampton, Virginia 23665-5225
February 29, 1988

References

1. Schmitz, F. H.; and Boxwell, D. A.: In-Flight Far-Field Measurement of Helicopter Impulsive Noise. Preprint No. 1062, *Proceedings of the 32nd Annual National V/STOL Forum,* American Helicopter Soc., Inc., May 1976.
2. Boxwell, D. A.; and Schmitz, F. H.: Full-Scale Measurements of Blade-Vortex Interaction Noise. Preprint No. 80-61, *Proceedings of the 36th Annual Forum,* American Helicopter Soc., Inc., May 1980.
3. Charles, Bruce D.: Acoustic Effects of Rotor-Wake Interaction During Low-Power Descent. *Proceedings of the National Symposium on Helicopter Aerodynamic Efficiency,* American Helicopter Soc., Inc., 1975, pp. 7-1–7-8.
4. Tangler, James L.: Schlieren and Noise Studies of Rotors in Forward Flight. *Proceedings of the 33rd Annual National Forum,* American Helicopter Soc., Inc., May 1977, pp. 77.33-05-1–77.33-05-12.
5. Splettstoesser, W. R.; Schultz, K. J.; Boxwell, D. A.; and Schmitz, F. H.: *Helicopter Model Rotor-Blade Vortex Interaction Impulsive Noise: Scalability and Parametric Variations.* NASA TM-86007, USAAVSCOM TM-84-A-7, 1984.
6. Hoad, Danny R.: Helicopter Model Scale Results of Blade-Vortex Interaction Impulsive Noise as Affected by Tip Modification. *Proceedings of the 36th Annual Forum,* American Helicopter Soc., Inc., May 1980, pp. 80-62-1–80-62-13.
7. Martin, R. M.; and Connor, Andrew B.: *Wind-Tunnel Acoustic Results of Two Rotor Models With Several Tip Designs.* NASA TM-87698, 1986.
8. Schlinker, Robert H.; and Amiet, Roy K.: *Rotor-Vortex Interaction Noise.* NASA CR-3744, 1983.
9. Ahmadi, Ali R.: *An Experimental Investigation of the Chopping of Helicopter Main Rotor Tip Vortices by the Tail Rotor.* NASA CR-177338, 1984.
10. Hubbard, J. E., Jr.; and Harris, W. L.: Model Helicopter Rotor Impulsive Noise. *J. Sound & Vib.*, vol. 78, no. 3, Oct. 8, 1981, pp. 425–437.
11. Leighton, Kenneth P.; and Harris, Wesley L.: *On Mach Number Scaling of Blade/Vortex Noise Produced by Model Helicopter Rotors at Moderate Tip Speeds.* FDRL Rep. 84-3, Dep. of Aeronautics and Astronautics, Massachusetts Inst. of Technology, Oct. 1984.
12. Boxwell, D. A.; Schmitz, F. H.; Splettstoesser, W. R.; Schultz, K. J.; Lewy, S.; and Caplot, M.: *A Comparison of the Acoustic and Aerodynamic Measurements of a Model Rotor Tested in Two Anechoic Wind Tunnels.* NASA TM-88364, USAAVSCOM TM-86-A-6, 1986.
13. Martin, R. M.; Splettstoesser, W. R.; Schultz, K.-J.; and Elliott, J. W.: *Acoustic Measurements From a Rotor Blade-Vortex Interaction Noise Experiment in the German-Dutch Wind Tunnel (DNW).* NASA TM-4024, AVSCOM TR 87-B-4, 1988.
14. Martin, Ruth M.; and Splettstoesser, Wolf R.: Acoustic Results of the Blade-Vortex Interaction Acoustic Test of a 40 Percent Model Rotor in the DNW. *Proceedings of the National Specialists' Meeting on Aerodynamics and Aeroacoustics,* American Helicopter Soc., c.1987.
15. Van Ditshuizen, J. C. A.; Courage, G. D.; Ross, R.; and Schultz, K.-J.: Acoustic Capabilities of the German-Dutch Wind Tunnel (DNW). AIAA-83-0146, Jan. 1983.
16. *Compilation of Calibration Data of the German-Dutch Wind Tunnel.* MP-82.01, Duits-Nederlandse Windtunnel, Mar. 13, 1982.
17. Ross, R.; Van Nunen, J. W. G.; Young, K. J.; Allen, R. M.; and Van Ditshuizen, J. C. A.: *Aero-Acoustic Calibration of DNW Open Jet.* DNW TR 82.03, German-Dutch Windtunnel (DNW) (North East Polder, Netherlands), July 1982. (Also available as Boeing Document D6-51501, 1983.)
18. Seidel, M.; and Maarsingh, R. A.: Test Capabilities of the German-Dutch Wind Tunnel DNW for Rotors, Helicopters and V/STOL Aircraft. *Proceedings of the Fifth European Rotorcraft and Powered Lift Aircraft Forum,* Sept. 1979, pp. 17-1–17-22.

19. Langer, H. J. (SCITRAN, transl.): *DFVLR Rotorcraft—Construction and Engineering.* NASA TM-77740, 1984.
20. Langer, H.-J. (Leo Kanner Assoc., transl.): *Data Input, Processing and Presentation.* NASA TM-77739, 1984.
21. Breustedt, Wolfgang (SCITRAN, transl.): *Data Analysis on the Rotor Test Stand Program for Interactive Processing.* NASA TM-77948, 1985.
22. Applin, Zachary T.: Modification to the NASA Langley 4- by 7-Meter Tunnel for Improved Rotorcraft Aerodynamics and Acoustics. NASA paper presented at the American Helicopter Society National Specialists' Meeting on Helicopter Testing Technology (Williamsburg, Va.), Oct. 29–Nov. 1, 1984.
23. Heyson, Harry H.: *Use of Superposition in Digital Computers To Obtain Wind-Tunnel Interference Factors for Arbitrary Configurations, With Particular Reference to V/STOL Models.* NASA TR R-302, 1969.
24. Peterson, Arnold P. G.: *Handbook of Noise Measurement,* Ninth ed. GenRad, Inc., 1980.
25. Splettstoesser, W. R.; Schultz, K. J.; and Martin, Ruth M.: Rotor Blade-Vortex Interaction Impulsive Noise Source Identification and Correlation With Rotor Wake Predictions. AIAA-87-2744, Oct. 1987.
26. Hoad, Danny R.: *Evaluation of Helicopter Noise Due to Blade-Vortex Interaction for Five Tip Configurations.* NASA TP-1608, 1979.
27. Martin, R. M.; Elliott, J. W.; and Hoad, D. R.: Comparison of Experimental and Analytical Predictions of Rotor Blade-Vortex Interactions Using Model Scale Acoustic Data. AIAA-84-2269, Oct. 1984.
28. Landgrebe, Anton J.: Overview of Helicopter Wake and Airloads Technology. *Proceedings of the Twelfth European Rotorcraft Forum,* American Helicopter Soc., Sept. 1986, pp. 18-1–18-32.
29. Widnall, Sheila: Helicopter Noise Due to Blade-Vortex Interaction. *J. Acoust. Soc. America,* vol. 50, no. 1, pt. 2, July 1971, pp. 354–365.
30. Hoad, Danny R.: *Helicopter Blade-Vortex Interaction Locations—Scale-Model Acoustics and Free-Wake Analysis Results.* NASA TP-2658, AVSCOM TM 87-B-1, 1987.

Table I. Details of the BO-105 Model Main Rotor and Rotor Test Stand

Main rotor:	
Rotor diameter, m	4
Blade airfoil section	NACA 23012
Number of blades	4
Blade solidity	0.077
Blade tip speed, m/sec	218
Flapping frequency ratio	1.111
Lagging frequency ratio	0.785
Nominal rotational speed, rpm	1040
Nominal rotor thrust, N	3600
Nominal rotor thrust coefficient	0.0044
Drive system:	
Shaft power, kW	100
Rotor drive moment, N-m	900 at 1050 rpm
Power (electric)	3 phase, 380 V at 300 A
Balance load range:	
Axial force, N	1000
Side force, N	2000
Thrust force, N	7000 static ±1500 dynamic
Rolling moment, N-m	700
Pitching moment, N-m	700
Control system:	
Blade setting angle range, deg	−4 to 14

Table II. Exploratory Test Matrix

Comment	C_T	V, m/sec	μ	α_{shaft}, deg	X_w, m	Z_w, m
μ sweep	0.0044	20 to 40	0.092 to 0.184	0	4.0	−2.1
				2		
				4		
				6		
				8		
				10		
X_w sweep	0.0044	37	0.170	0	6.0 to −0.7	−2.1
		32	.147	2		
		30	.138	4		
		25	.115	6		
		20	.092	8		
		17	.078	10		
μ sweep	0.0030	20 to 40	0.092 to 0.184	−1	−1.0	−2.1
				1		
				3		
X_w sweep	0.0030	40	0.184	1	4.0 to −1.0	−2.1
		30	.138	3		
		30	.138	5		

Table III. Final Test Matrix

Comment	C_T	V, m/sec	μ	α_{shaft}, deg	X_w, m	Z_w, m	M_H
α sweep	0.0044	17	0.078	[a]7 to 10	5.0	−2.1	0.636
		20	.092	6 to 10	2.5		
		25	.115	4 to 8	2.5		
		30	.138	2 to 4	1.0		
		32	.147	0 to 4	1.0		
		37	.170	−2 to 2	2.5		
μ sweep	0.0044	[b]33 to 41	0.152 to 0.187	0	2.5	−2.1	0.636
		28 to 36	0.129 to 0.166	2.0	1.0		
		25 to 35	0.115 to 0.161	4.0	1.0		
		20 to 26	0.092 to 0.120	6.0	2.5		
		17 to 22	0.078 to 0.101	8.0	2.5		
		13 to 21	0.060 to 0.097	10.0	5.0		
X_w sweep	0.0044	38	0.175	0.5	[c]6.0 to −1.2	−2.1	0.636
		35	.161	3.0			
		31	.143	5.0			
		25	.115	5.5			
		20	.092	8.0			
		19	.087	10.0			
α sweep	0.0044	30	0.138	[a]4 to 7	−1.15	−2.1	0.636
μ sweep	0.0044	[b]28 to 34	0.129 to 0.156	5.0	−1.15	−2.1	0.636
X_w sweep	0.0044	30	0.138	5.0	[d]4.4 to −1.2	−2.1	0.636
α sweep	0.0030	30	0.138	[a]1 to 7	−1.15	−2.1	0.636
		40	.184	−1 to 3			
μ sweep	0.0030	[b]28 to 35	0.129 to 0.161	2.8	−1.15	−2.1	0.636
		36 to 44	0.166 to 0.202	1.2			
X_w sweep	0.0030	30	0.138	2.8	[d]4.4 to −1.2	−2.1	0.636
		40	.184	1.2			
Near/far-field data	0.0044	19	0.087	10.0	[e]1.5 to 6.0	−1.6	0.636
		31	.143	5.0	[e]1.5 to 6.0	−1.6	
		19	.087	10.0	[f]2.5 to 6.2	−2.6	
		31	.143	5.0	[f]2.5 to 6.2	−2.6	
High μ	0.0044	50	0.230	−5 to 1	2.5	−2.1	0.636
		60	.276	−7 to 1	2.5	−2.1	
		60	.276	−7 to 0	2.57	−2.6	
		60	.276	−7 to 0	3.68	−2.6	
M_H sweep	0.0044	[g]27 to 35	0.140	5.0	4.5	−2.1	[h]0.56 to 0.72
C_T sweep	0.0036 to 0.0056	31	0.140	5.0	4.5	−2.1	0.636
M_H sweep	0.0044	[g]17.5 to 22.5	0.090	8.0	4.0	−2.1	[h]0.56 to 0.72
C_T sweep	0.0036 to 0.0056	20	0.090	8.0	4.0	−2.1	0.636
M_H sweep	0.0044	[g]33.3 to 42.8	0.175	0.5	4.0	−2.1	[h]0.56 to 0.72
C_T sweep	0.0036 to 0.0056	38	0.175	0.5	4.0	−2.1	0.636

[a]Varied in increments of 0.5.
[b]Varied in increments of 1.
[c]Varied as follows: 6.0, 5.2, 4.4, 3.6, 2.8, 2.0, 1.5, 0.8, 0, −0.7, −1.2.
[d]Varied as follows: 4.4, 2.8, 2.0, 1.2, 0.4, 0, −0.4, −0.7, −1.2.
[e]Varied as follows: 1.5, 2.1, 2.7, 3.3, 4.0, 4.6.
[f]Varied as follows: 2.5, 3.5, 4.4, 5.4, 6.2.
[g]Varied in increments of 2.
[h]Varied in increments of 0.04.

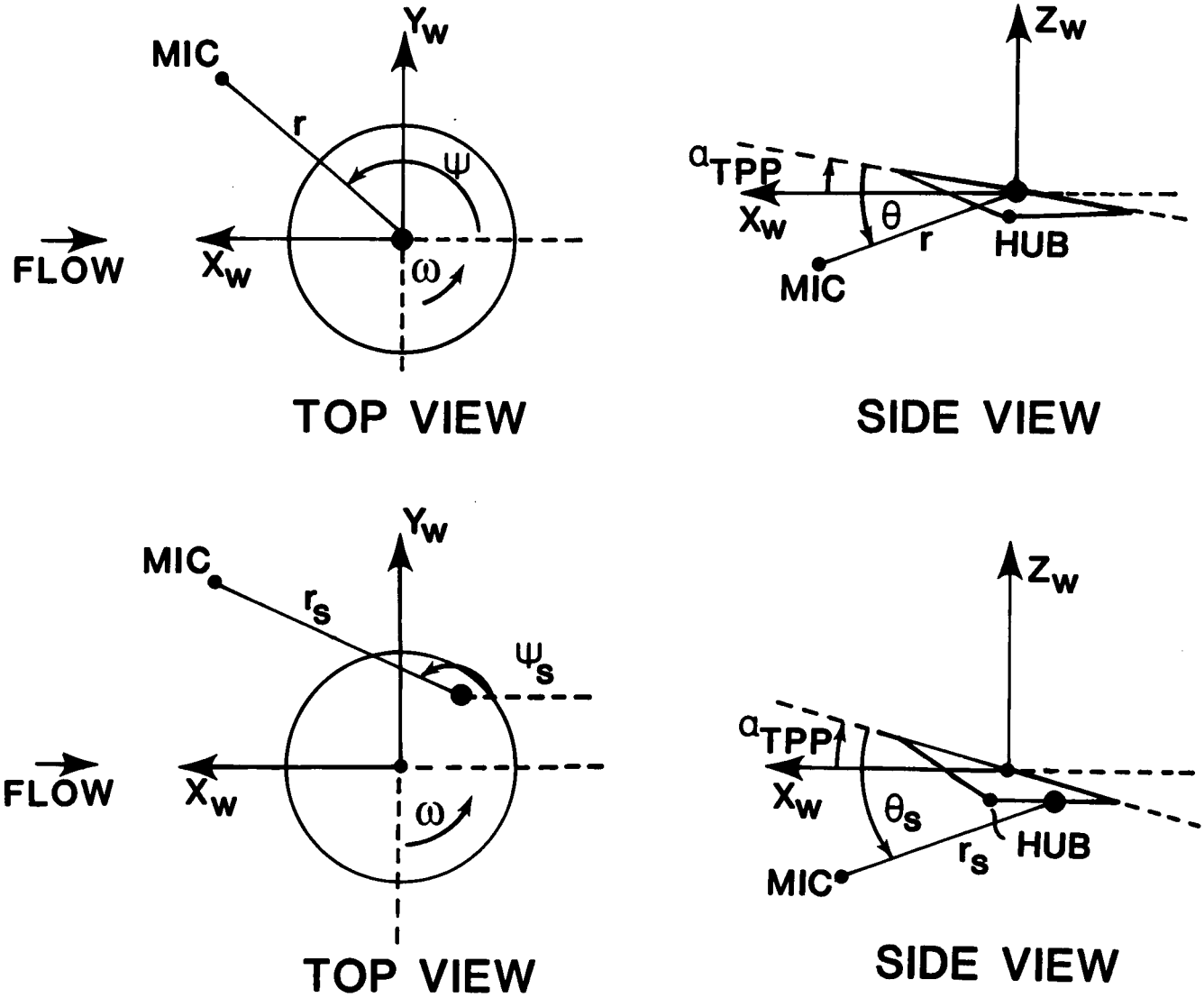

Figure 1. Diagram of coordinate system and test geometry.

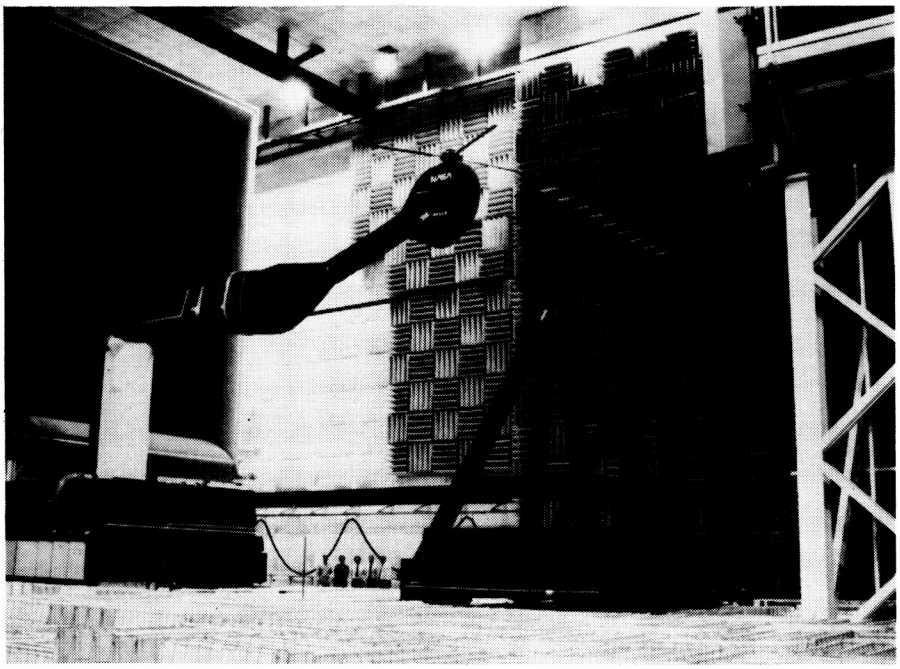

L-86-6263

(a) Side view.

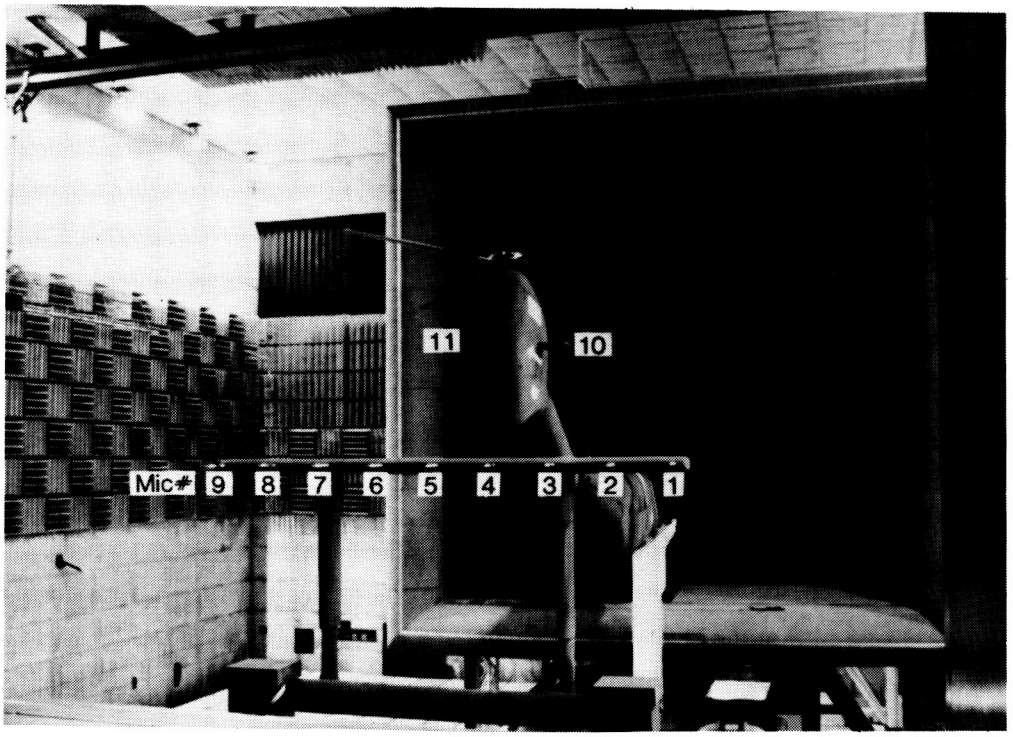

L-86-6243

(b) View looking downstream showing microphone numbers.

Figure 2. Experimental apparatus installed in the DNW open test section.

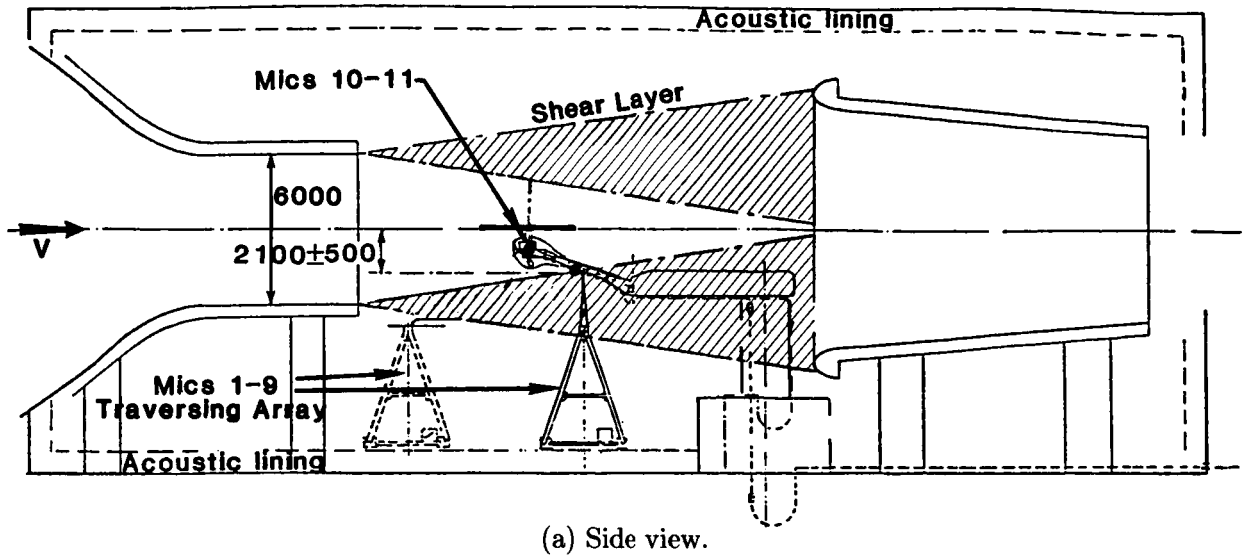

(a) Side view.

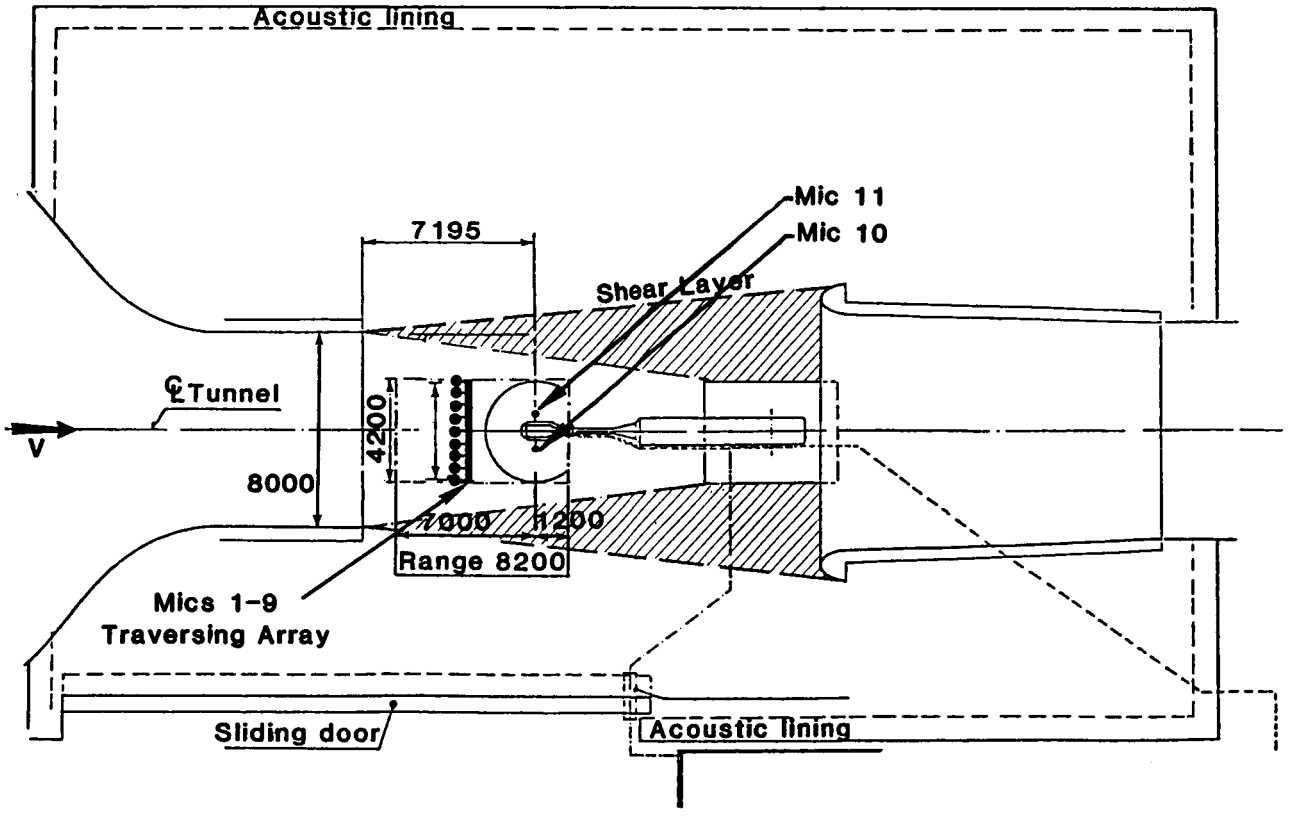

(b) Plan view.

Figure 3. Diagram of experimental apparatus installed in the DNW open test section. Dimensions are in millimeters.

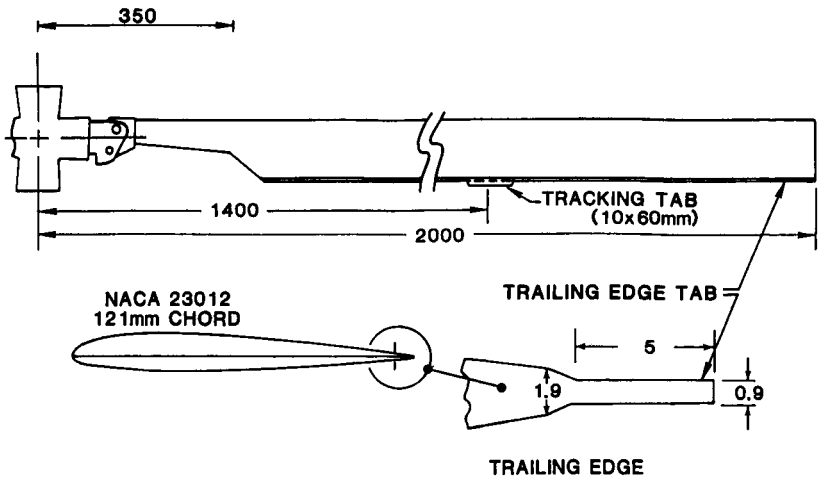

Figure 4. Model BO-105 rotor blade geometry. Dimensions are in milllimeters.

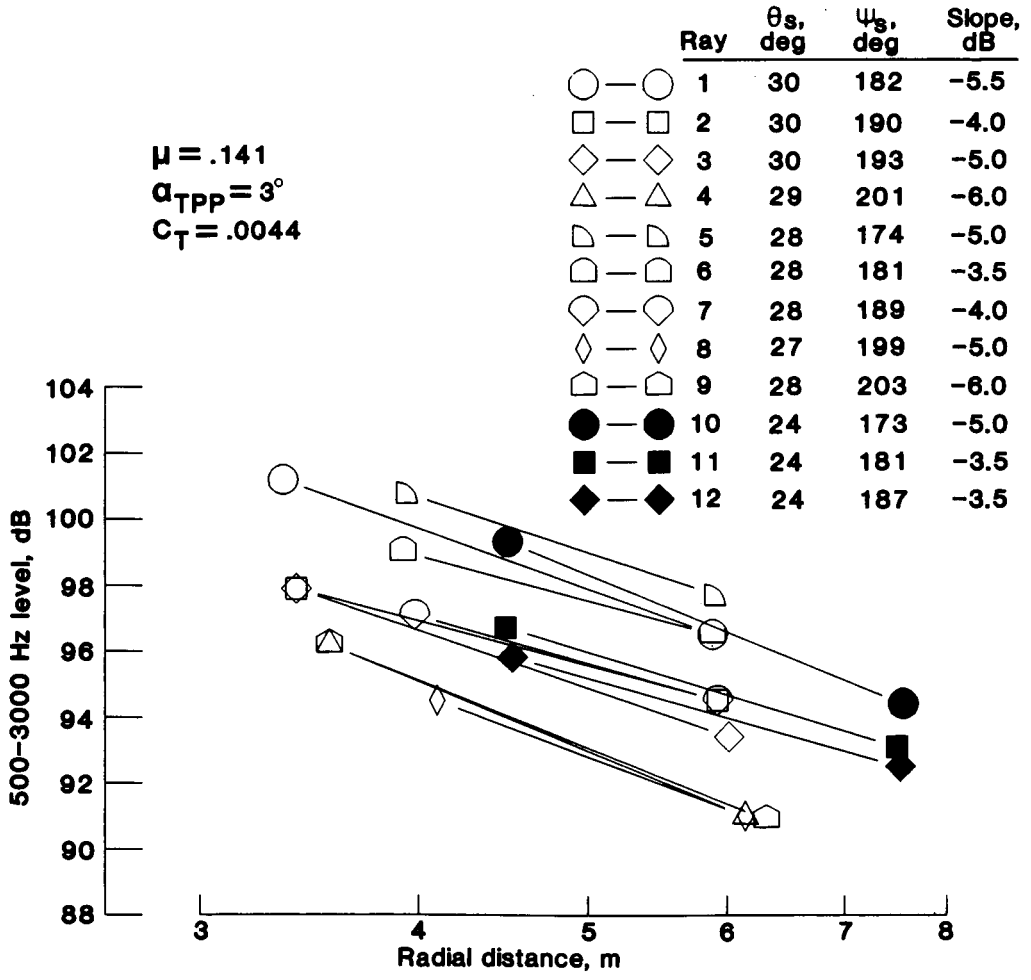

Figure 5. BVI spectral levels versus distance from source, measured at two locations on several acoustic rays.

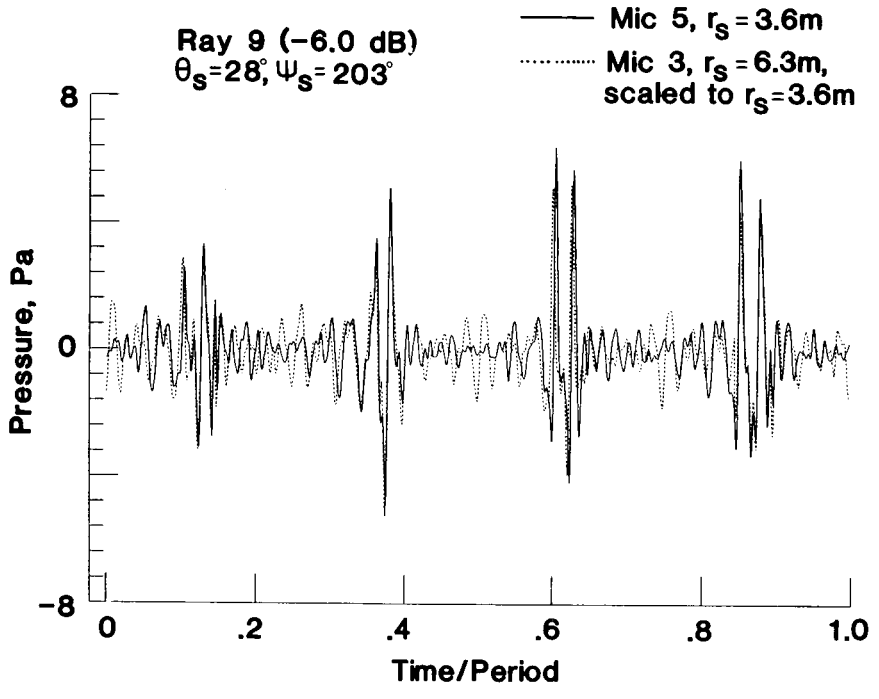

(a) Ray 9.

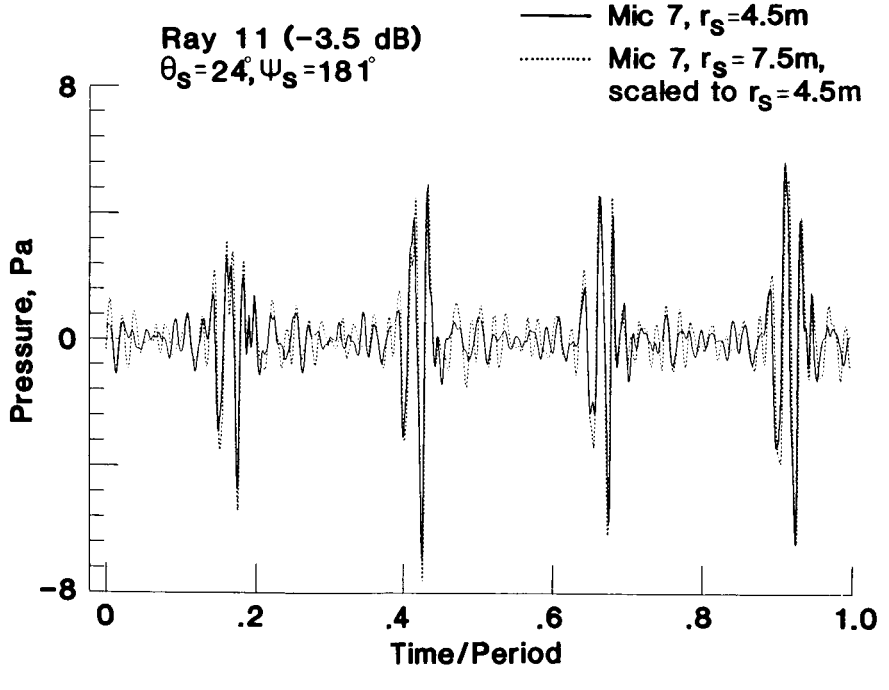

(b) Ray 11.

Figure 6. Comparison of filtered acoustic signals (500–3000 Hz) measured at two locations on same acoustic ray from source.

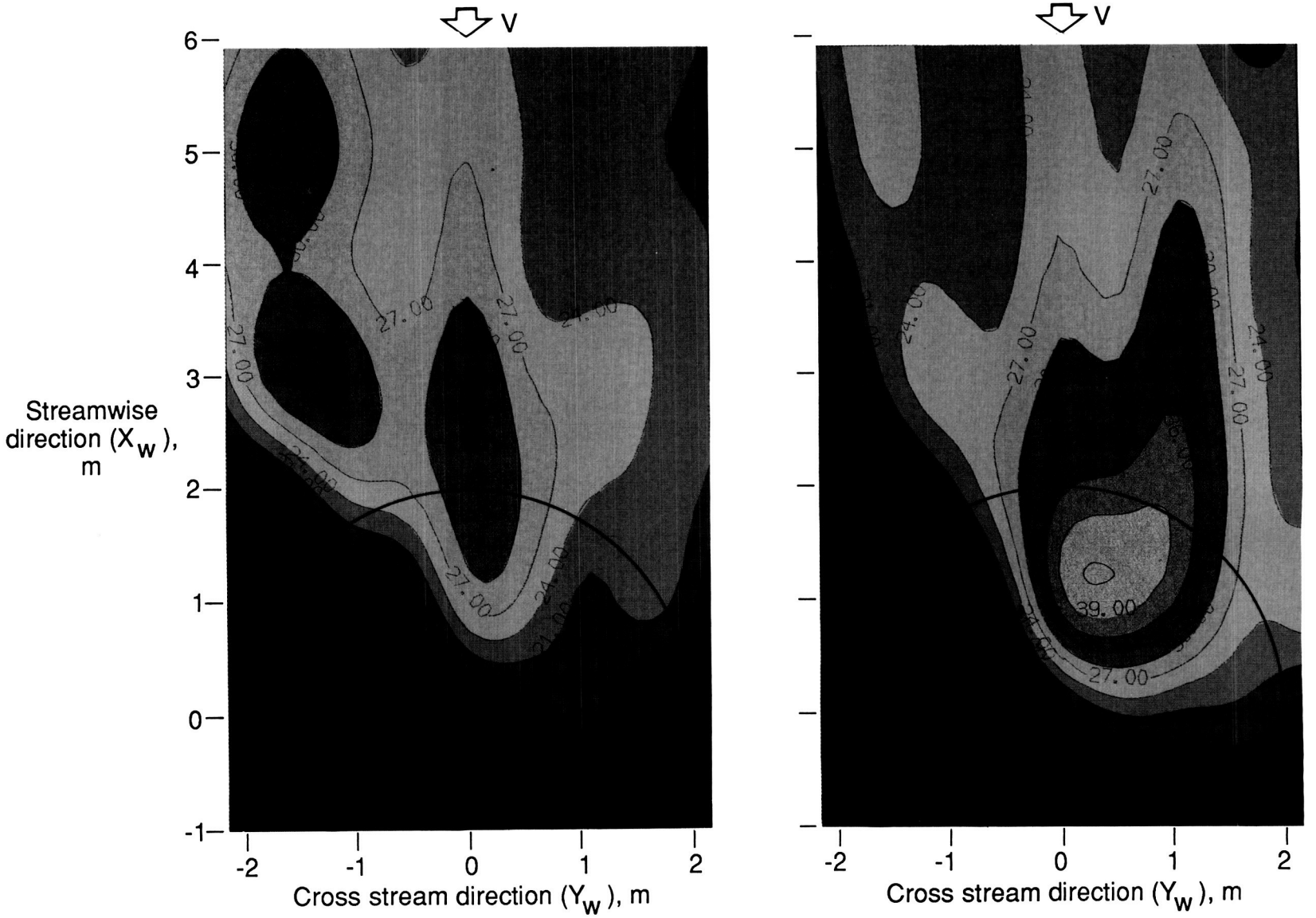

(a) $\mu = 0.075$; $\alpha_{\mathrm{TPP}} = 4.4°$.

(b) $\mu = 0.090$; $\alpha_{\mathrm{TPP}} = 3.9°$.

Figure 7. Contours (in PaN) of the filtered, averaged, blade-passage peak-to-peak pressure normalized to 4 m from BVI source at $r/R = 0.80$, $\psi = 60°$, and $C_{\mathrm{T}} = 0.0044$.

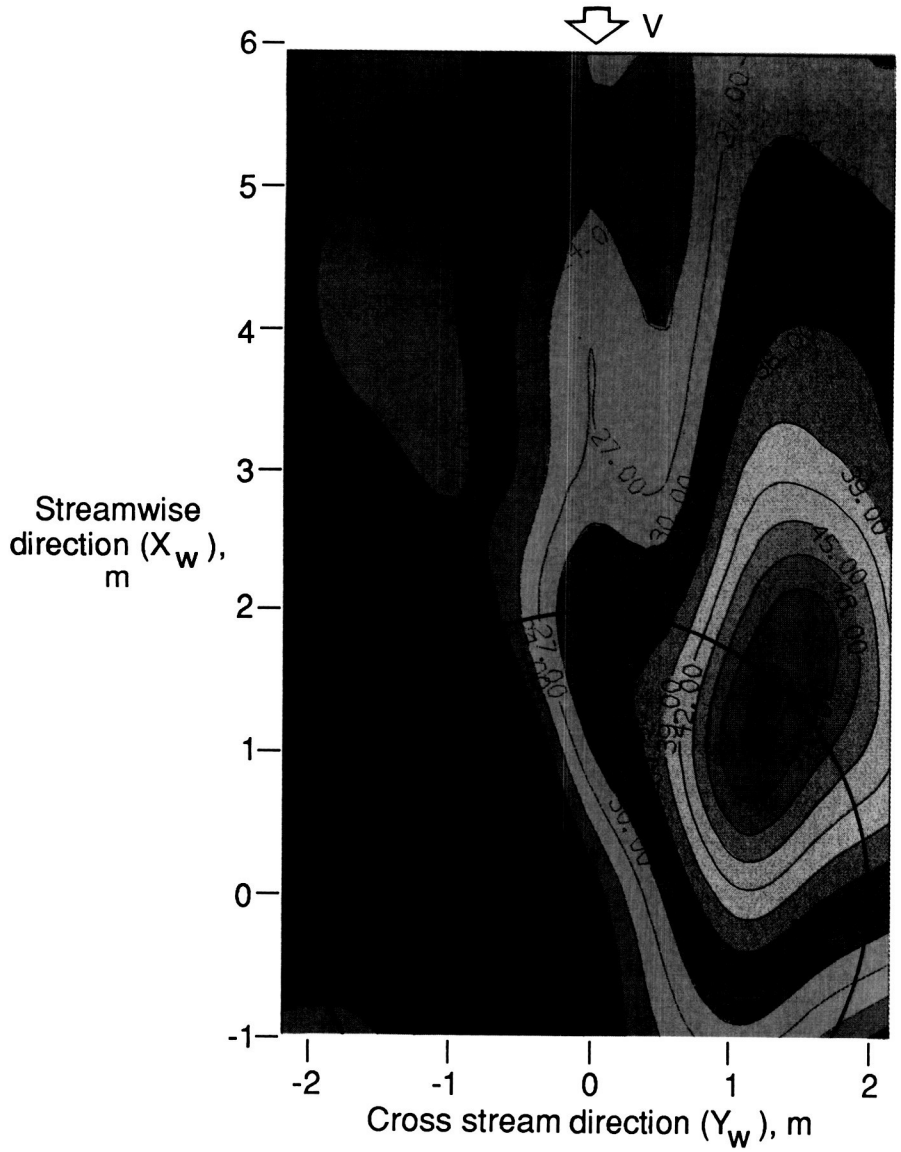

(c) $\mu = 0.116$; $\alpha_{TPP} = 3.4°$.

(d) $\mu = 0.138$; $\alpha_{TPP} = 2.3°$.

Figure 7. Continued.

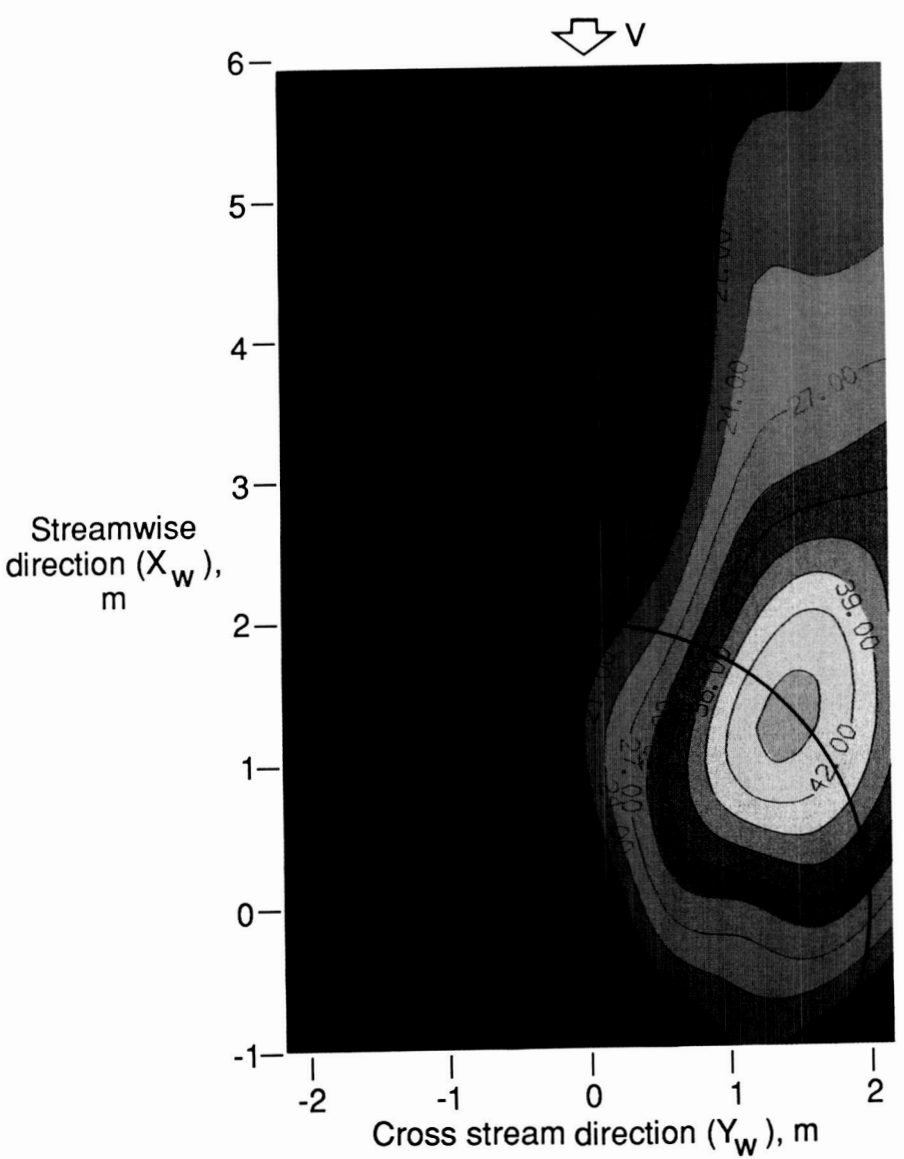

(e) $\mu = 0.146$; $\alpha_{TPP} = 0.5°$.

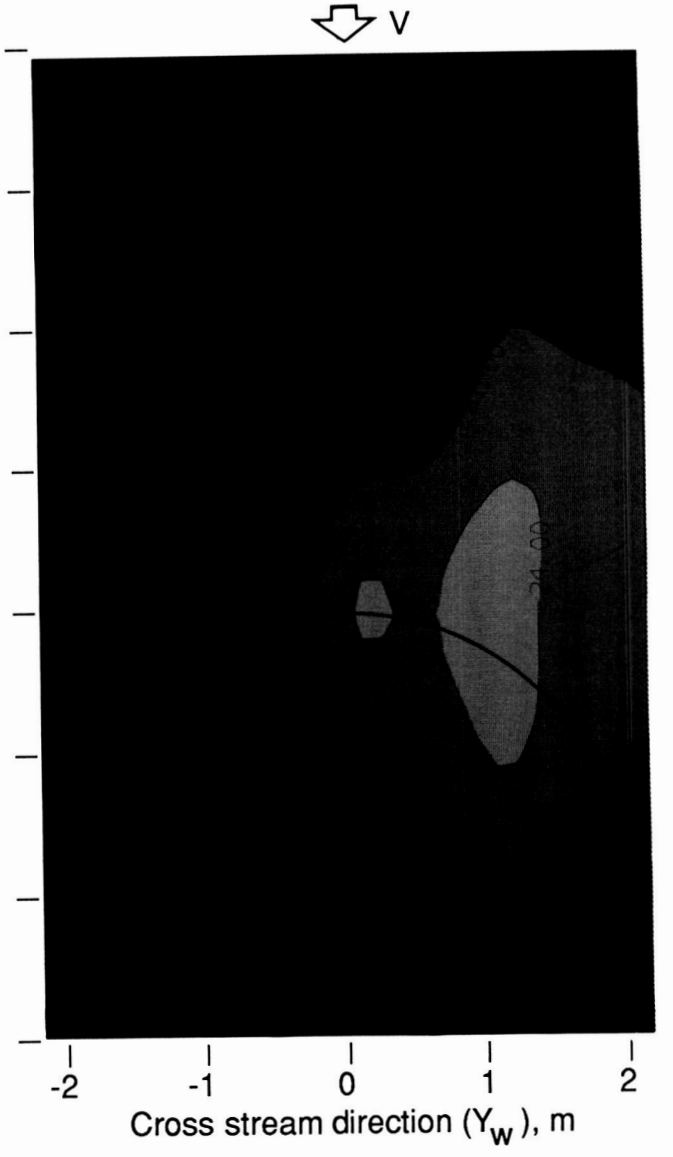

(f) $\mu = 0.170$; $\alpha_{TPP} = 1.1°$.

Figure 7. Concluded.

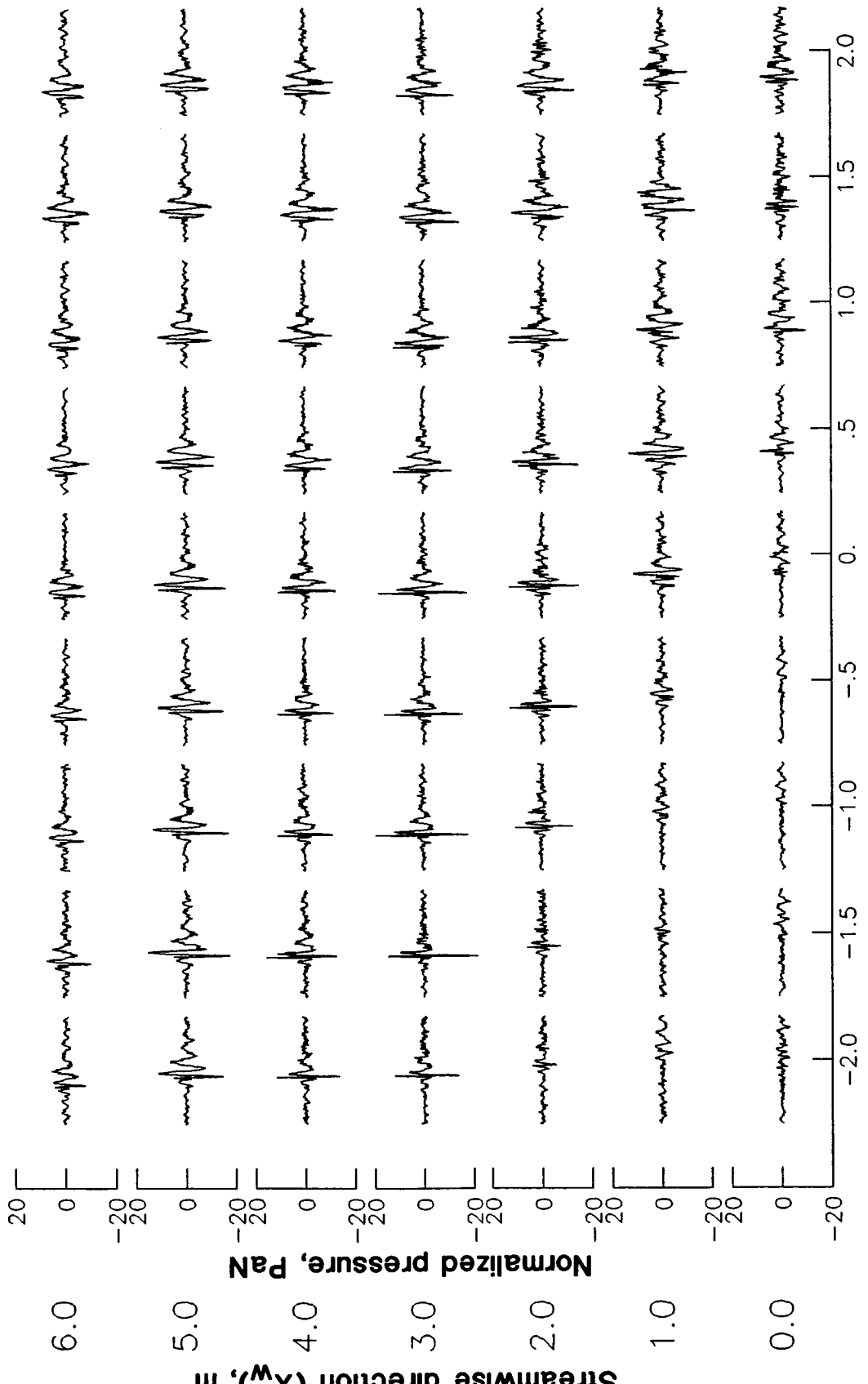

(a) $\mu = 0.075$; $\alpha_{TPP} = 4.4°$.

Figure 8. Example of one blade passage of unaveraged, filtered acoustic signals used to calculate directivity contours of figure 7.

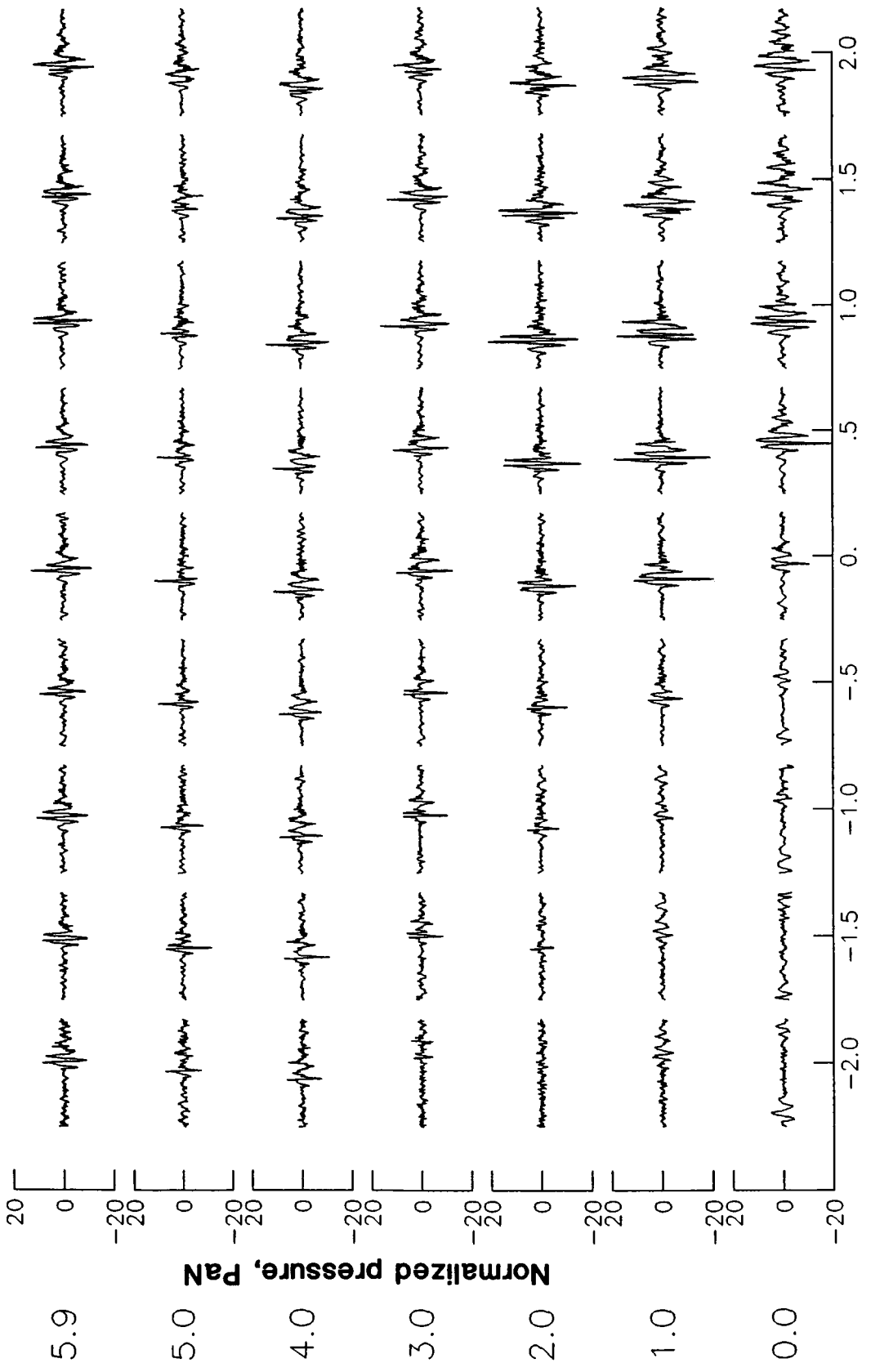

(b) $\mu = 0.090$; $\alpha_{\mathrm{TPP}} = 3.9°$.

Figure 8. Continued.

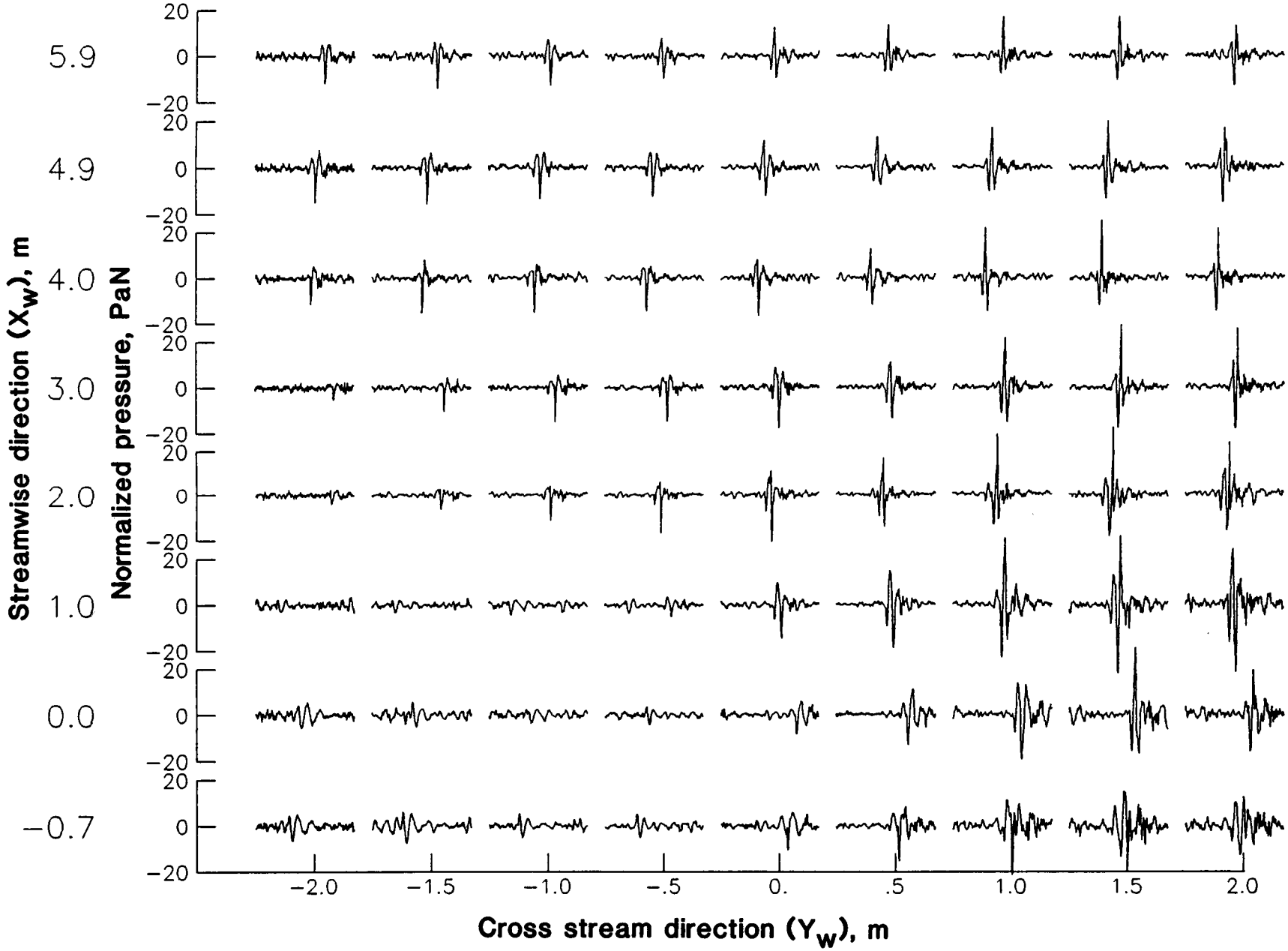

(c) $\mu = 0.116$; $\alpha_{TPP} = 3.4°$.

Figure 8. Continued.

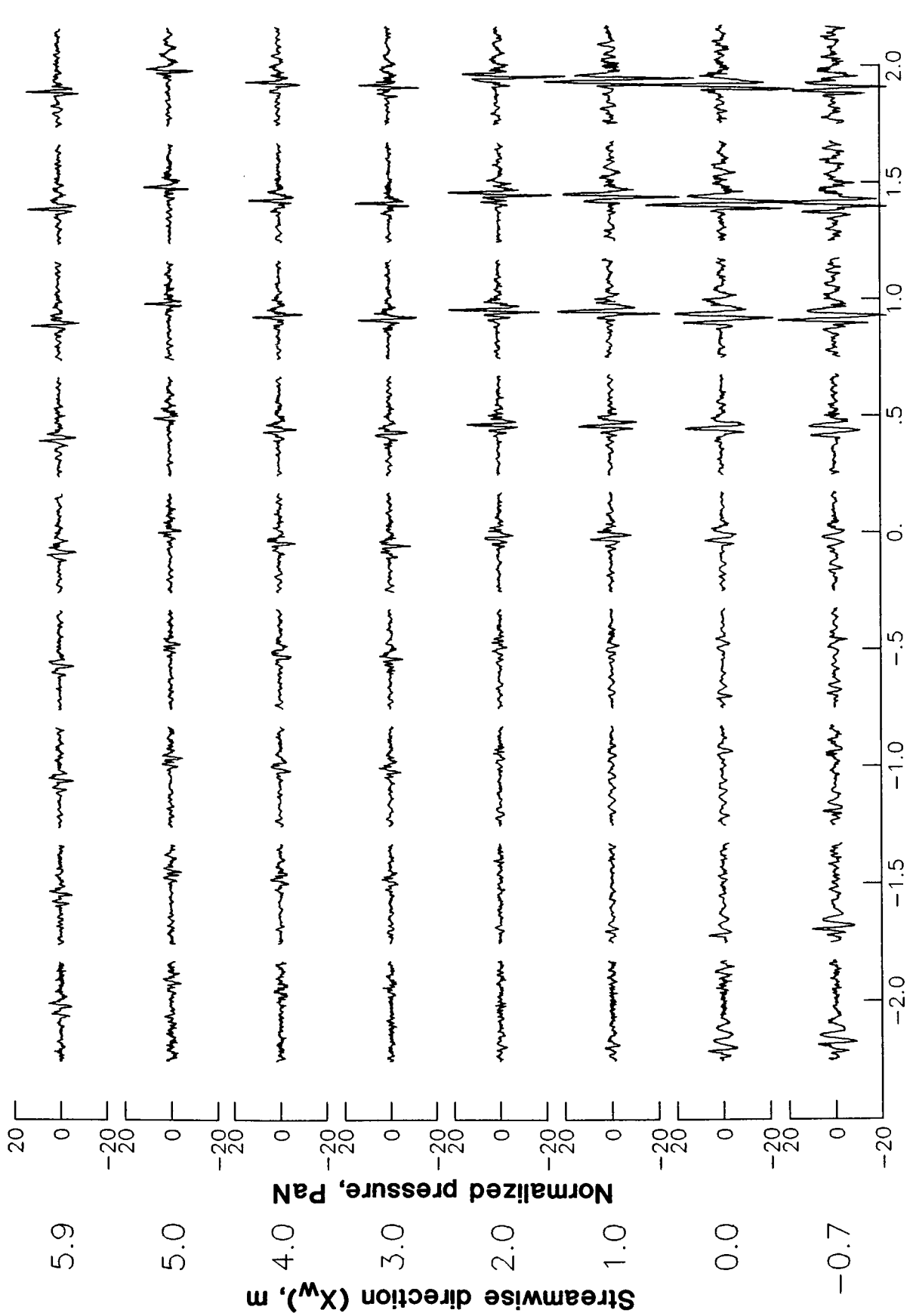

(d) $\mu = 0.138$; $\alpha_{TPP} = 2.3°$.

Figure 8. Continued.

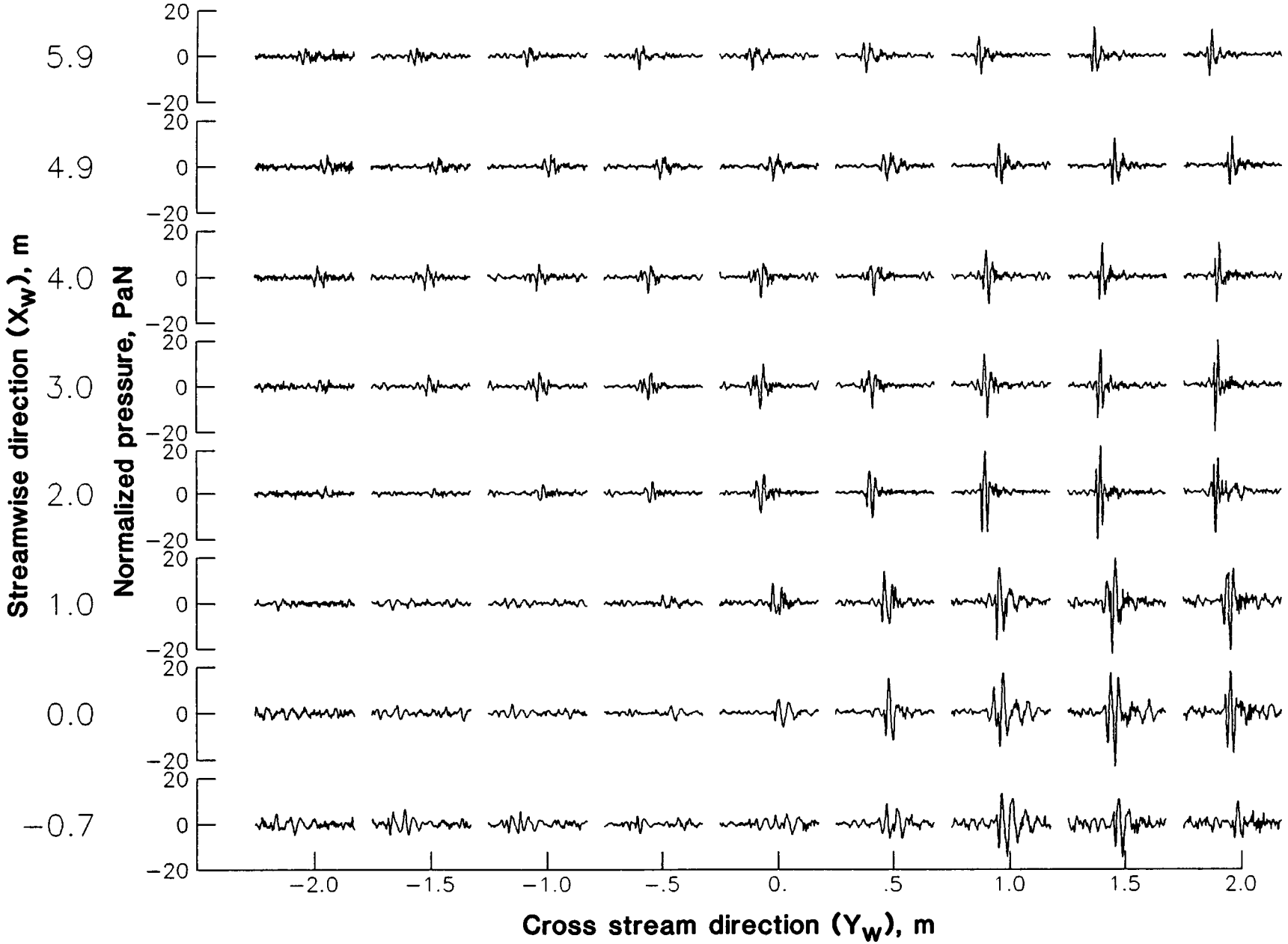

(e) $\mu = 0.146$; $\alpha_{TPP} = 0.5°$.

Figure 8. Continued.

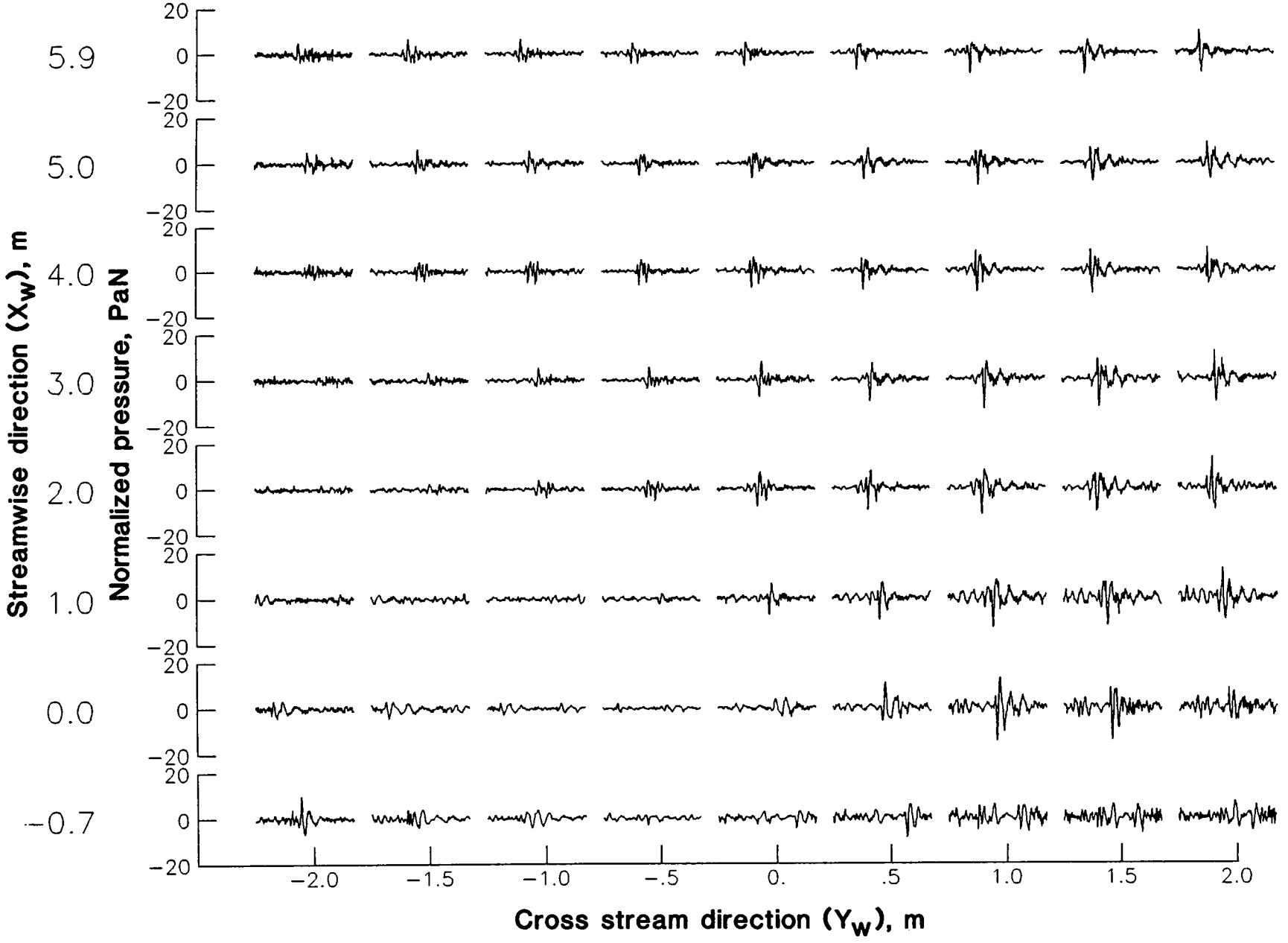

(f) $\mu = 0.170$; $\alpha_{TPP} = -1.1°$.

Figure 8. Concluded.

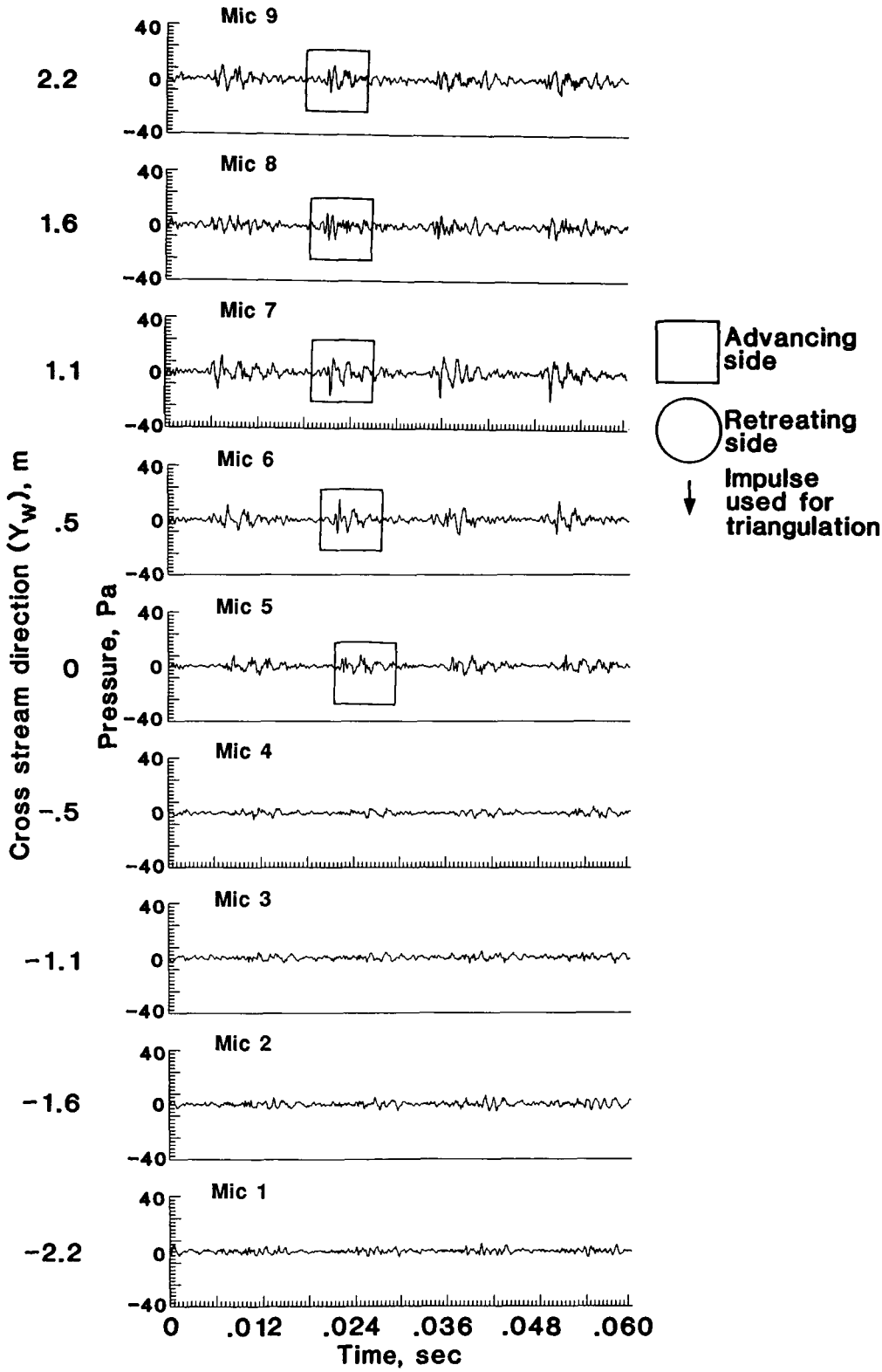

(a) $\mu = 0.075$; $\alpha_{TPP} = 4.4°$; $X_w = 0$ m.

Figure 9. Acoustic data measured under aft side of rotor exhibiting BVI from advancing and retreating side of disk. $C_T = 0.0044$.

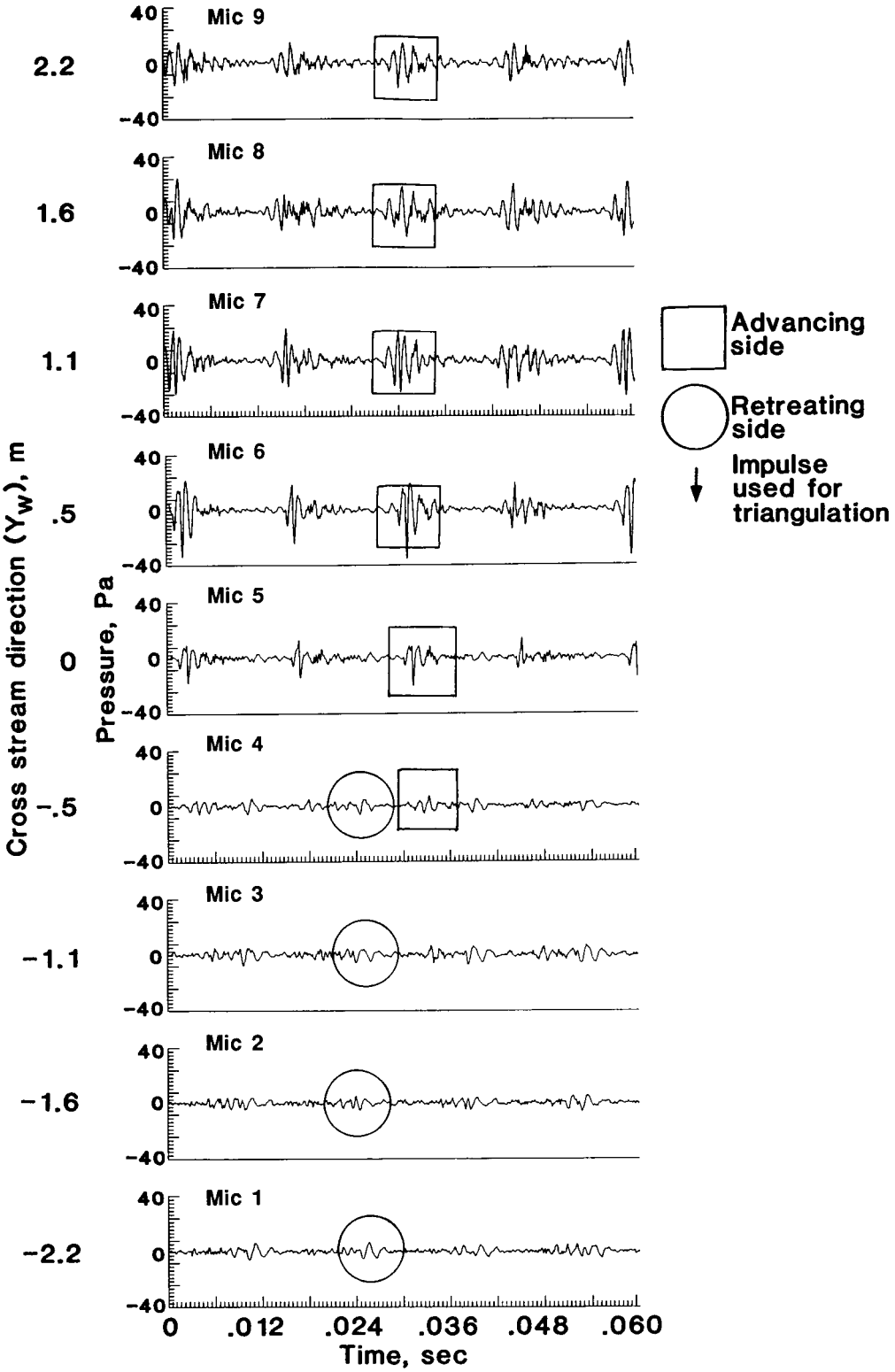

(b) $\mu = 0.090$; $\alpha_{TPP} = 3.9°$; $X_w = 0$ m.

Figure 9. Continued.

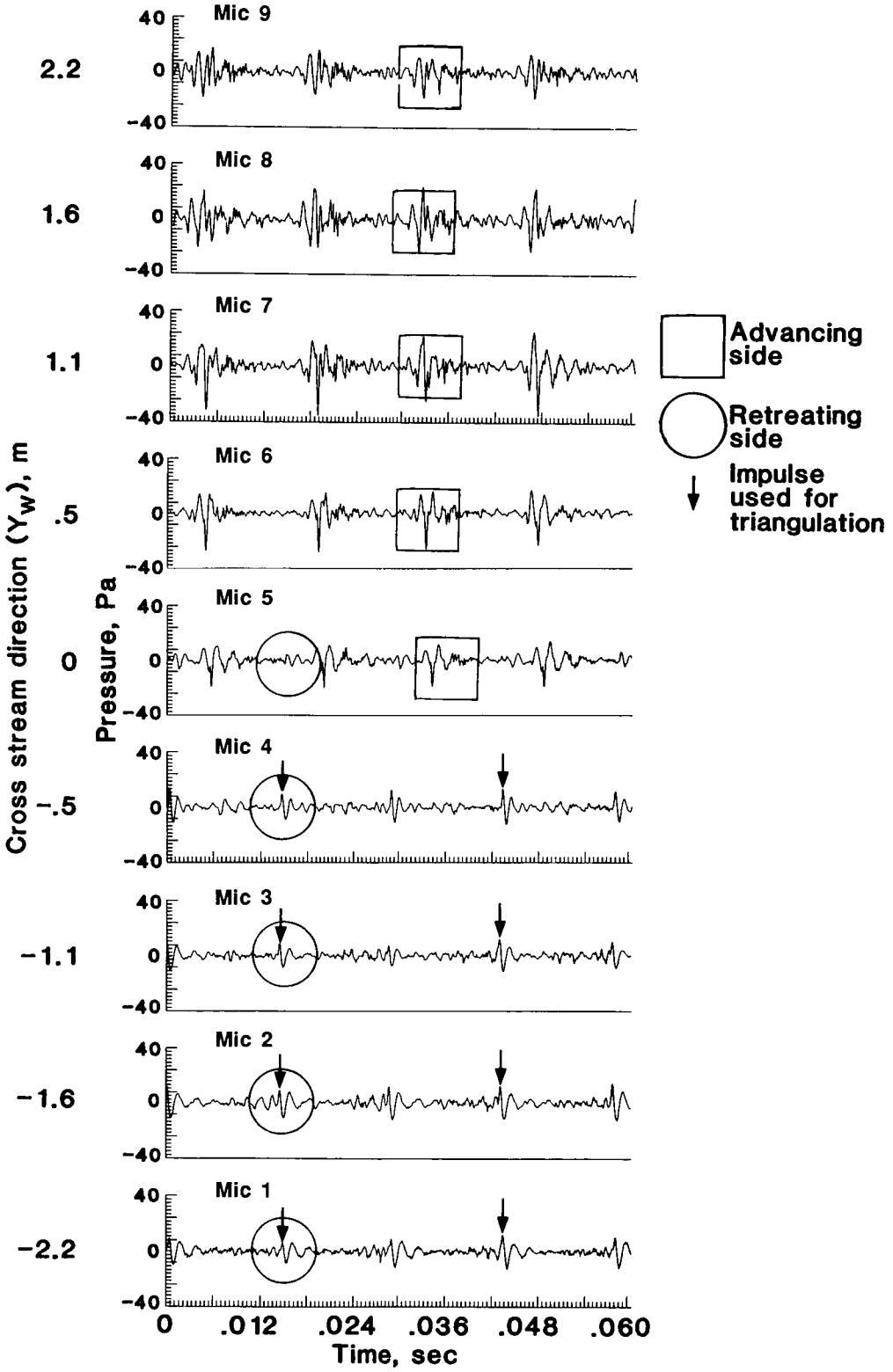

(c) $\mu = 0.116$; $\alpha_{TPP} = 3.4°$; $X_w = -0.7$ m.

Figure 9. Continued.

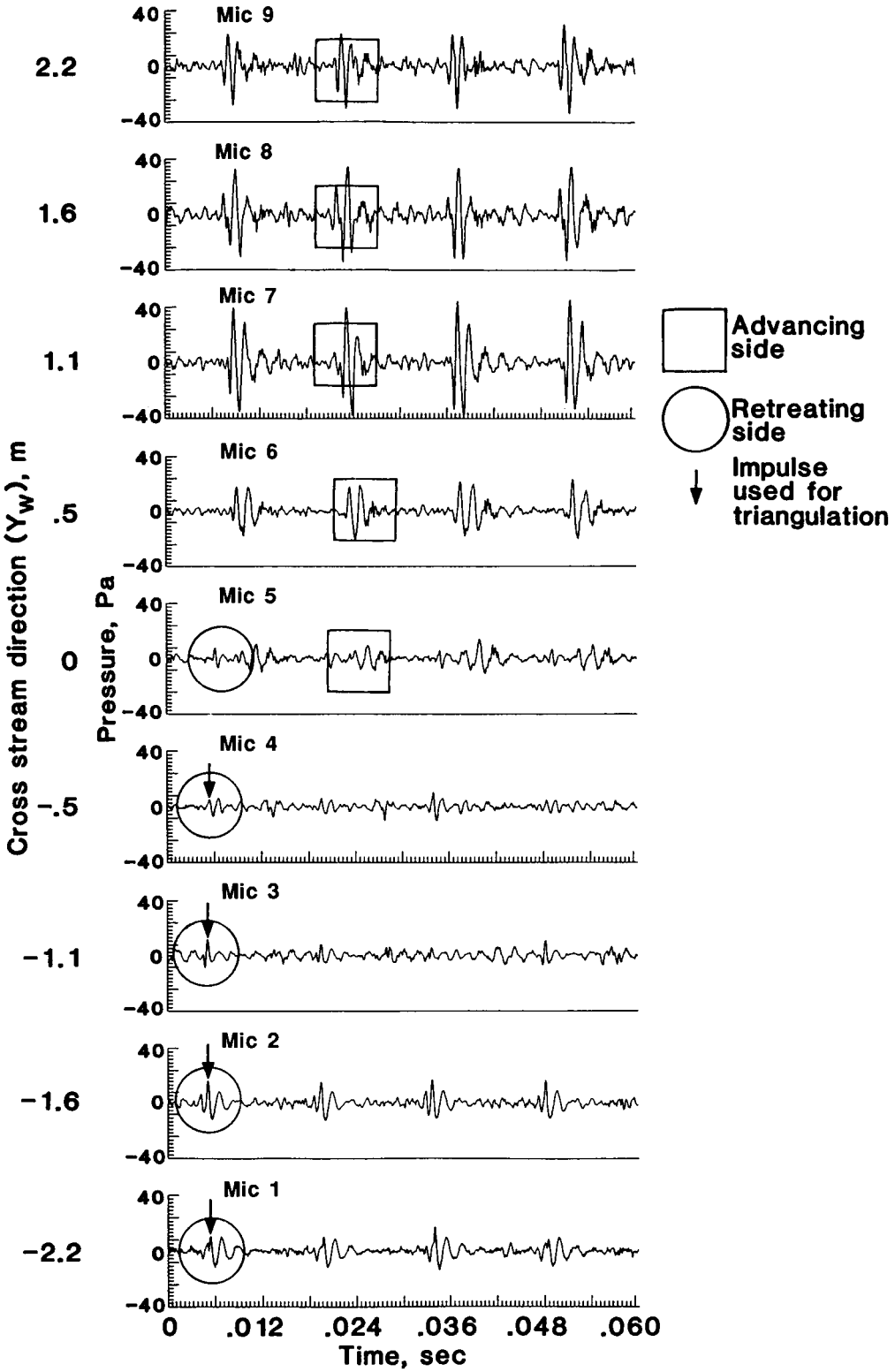

(d) $\mu = 0.138$; $\alpha_{TPP} = 2.3°$; $X_w = -0.7$ m.

Figure 9. Continued.

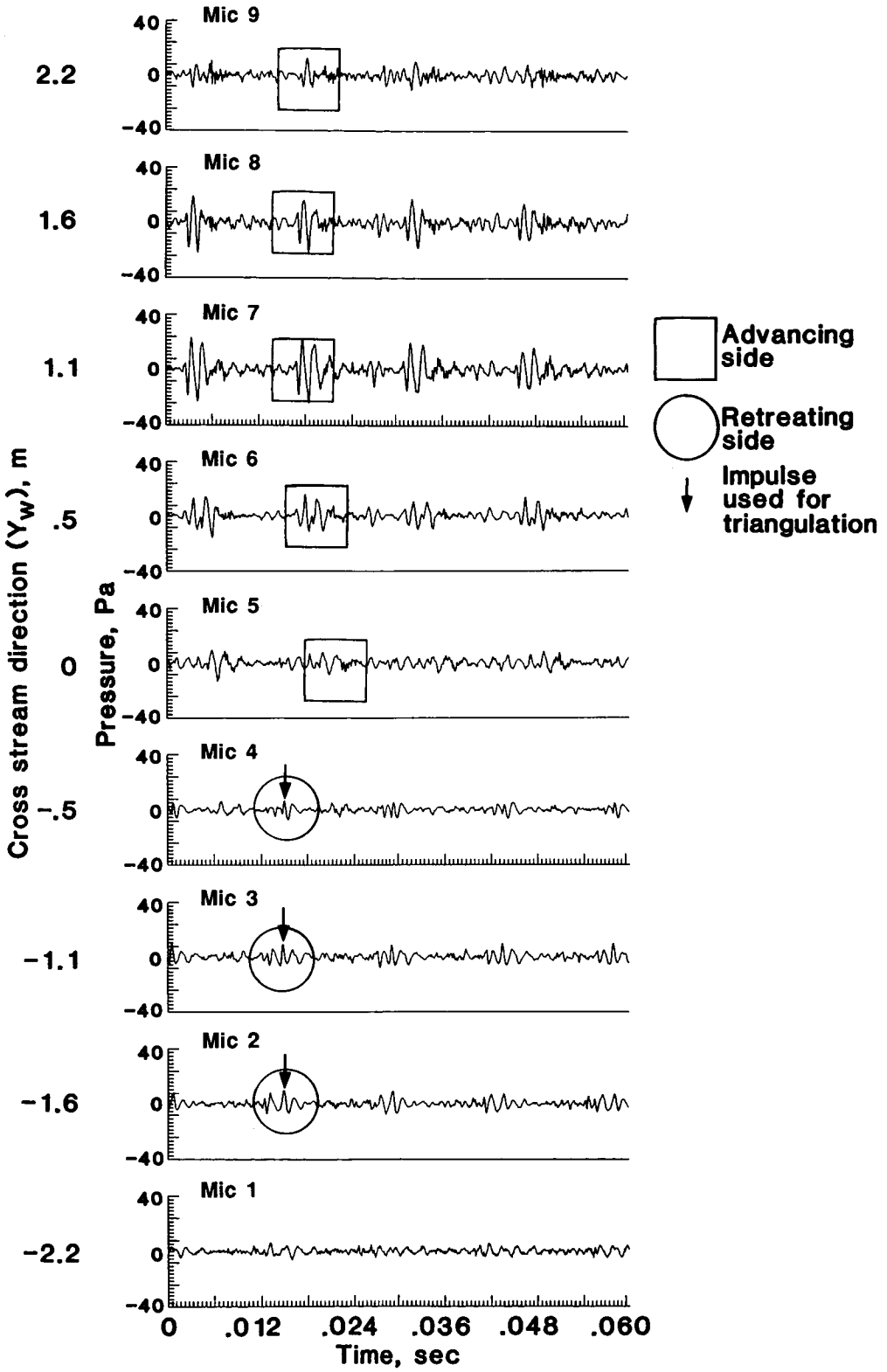

(e) $\mu = 0.146$; $\alpha_{TPP} = 0.5°$; $X_w = -0.7$ m.

Figure 9. Continued.

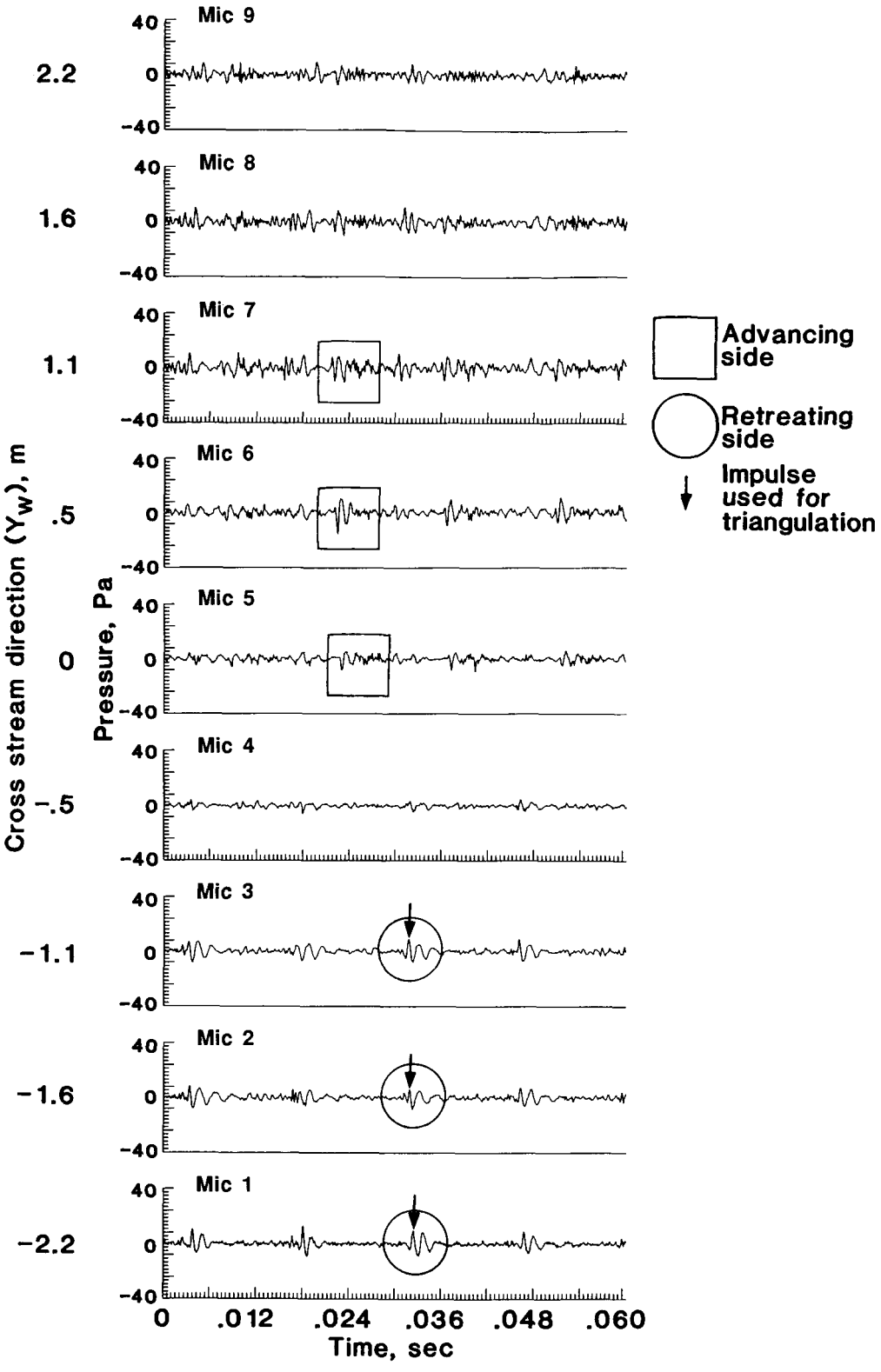

(f) $\mu = 0.170$; $\alpha_{TPP} = -1.1°$; $X_w = -0.7$ m.

Figure 9. Concluded.

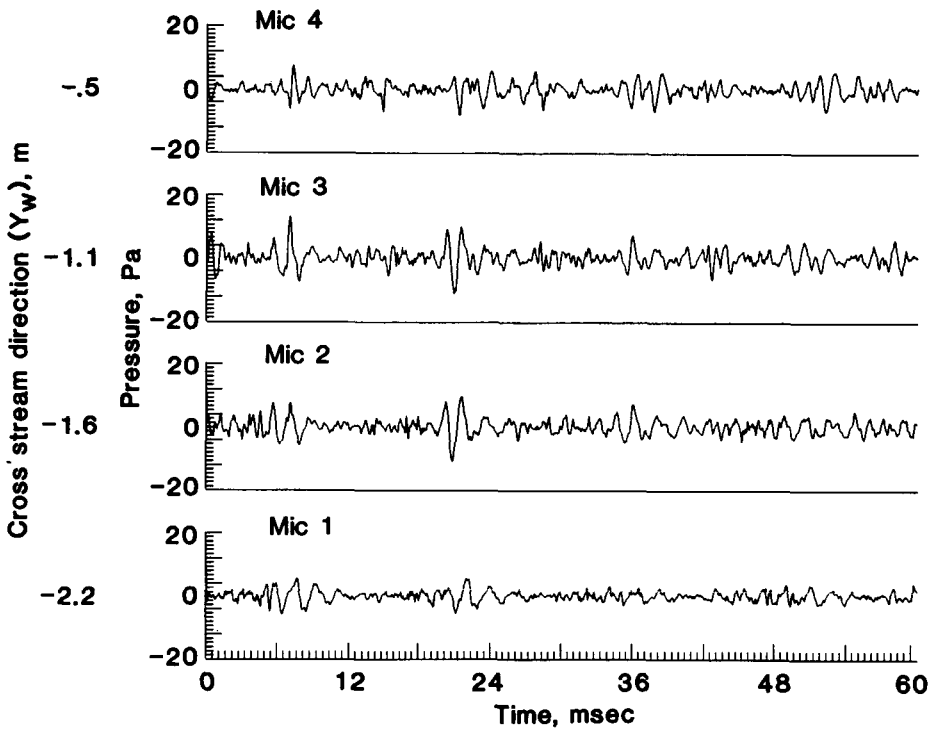

(a) $\mu = 0.138$; $\alpha_{\mathrm{TPP}} = 3.8°$; $X_w = -1.0$ m.

Figure 10. Acoustic data measured under retreating side of rotor exhibiting retreating-side BVI. $C_{\mathrm{T}} = 0.0030$.

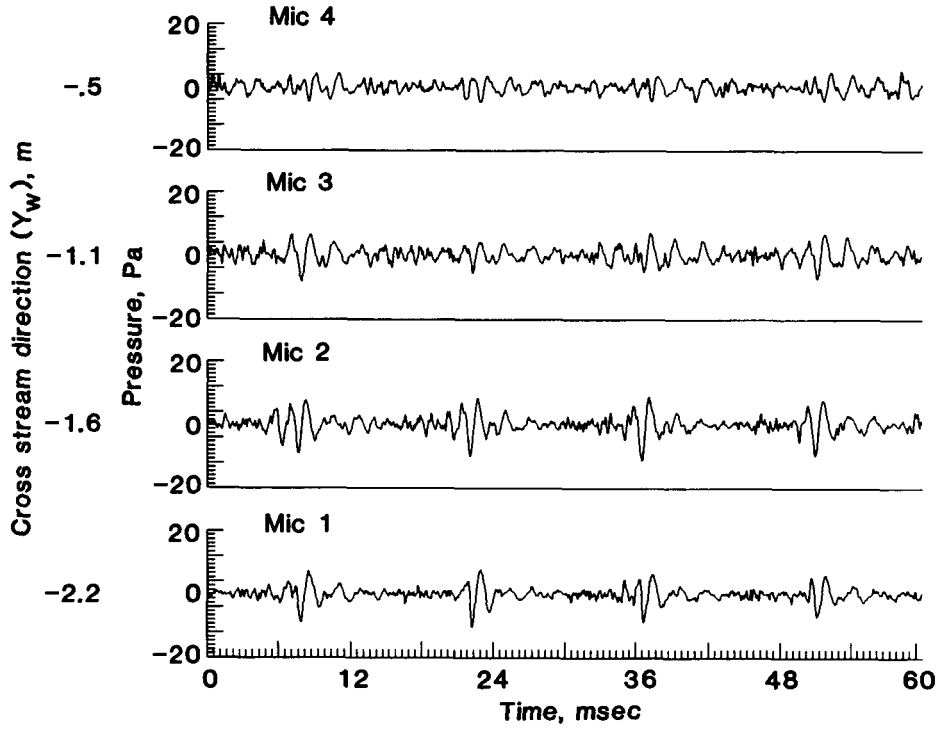

(b) $\mu = 0.138$; $\alpha_{\mathrm{TPP}} = 1.8°$; $X_w = -1.0$ m.

Figure 10. Continued.

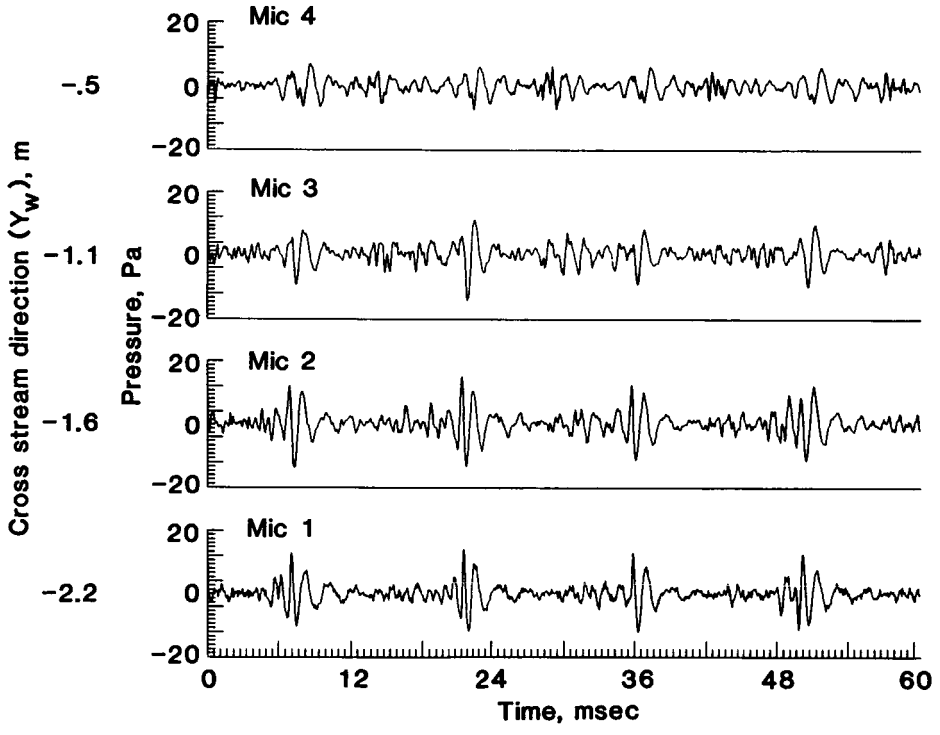

(c) $\mu = 0.184$; $\alpha_{TPP} = 0.4°$; $X_w = -0.5$ m.

Figure 10. Concluded.

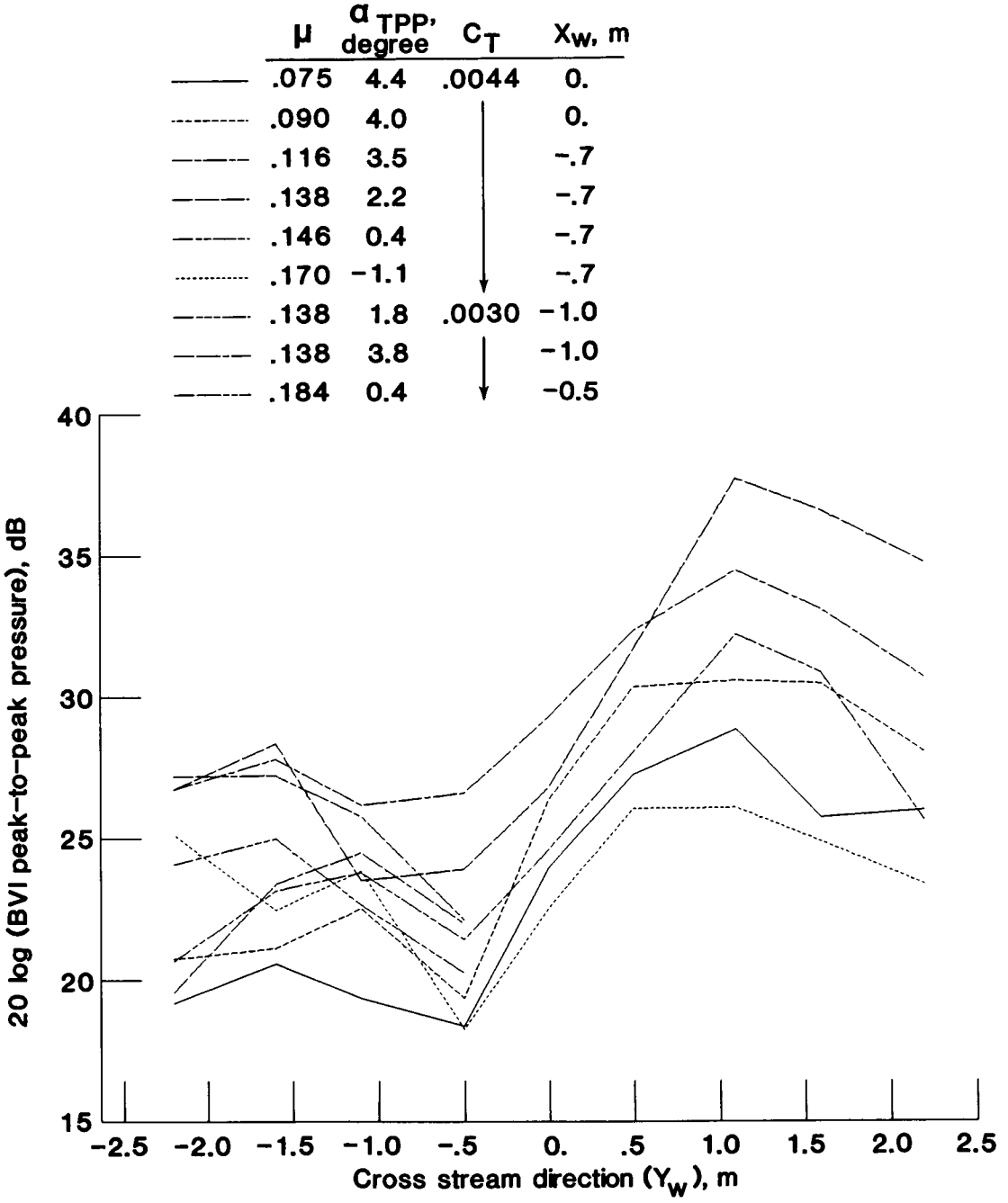

Figure 11. BVI acoustic metric (expressed in decibels) versus cross-stream position for data presented in figures 9 and 10.

NASA
National Aeronautics and Space Administration

Report Documentation Page

1. Report No.	2. Government Accession No.	3. Recipient's Catalog No.
NASA TP-2784 AVSCOM TR 87-B-3		

4. Title and Subtitle	5. Report Date
Advancing-Side Directivity and Retreating-Side Interactions of Model Rotor Blade-Vortex Interaction Noise	May 1988
	6. Performing Organization Code
7. Author(s)	8. Performing Organization Report No.
R. M. Martin, W. R. Splettstoesser, J. W. Elliott, and K.-J. Schultz	L-16354
9. Performing Organization Name and Address	10. Work Unit No.
NASA Langley Research Center Hampton, VA 23665-5225	505-61-51-06
	11. Contract or Grant No.
12. Sponsoring Agency Name and Address	13. Type of Report and Period Covered
National Aeronautics and Space Administration Washington, DC 20546-0001	Technical Paper
	14. Army Project No.

15. Supplementary Notes

R. M. Martin: Langley Research Center, Hampton, Virginia.
W. R. Splettstoesser and K.-J. Schultz: DFVLR, Braunschweig, West Germany.
J. W. Elliott: Aerostructures Directorate, USAARTA-AVSCOM, Langley Research Center, Hampton, Virginia.

16. Abstract

Acoustic data are presented from a 40-percent-scale model of the four-bladed BO-105 helicopter main rotor, tested in a large aeroacoustic wind tunnel. Rotor blade-vortex interaction (BVI) noise data in the low-speed flight range were acquired using a traversing in-flow microphone array. Acoustic results presented are used to assess the acoustic far field of BVI noise, to map the directivity and temporal characteristics of BVI impulsive noise, and to show the existence of retreating-side BVI signals. The characteristics of the acoustic radiation patterns, which can often be strongly focused, are found to be very dependent on rotor operating condition. The acoustic signals exhibit multiple blade-vortex interactions per blade with broad impulsive content at lower speeds, while at higher speeds, they exhibit fewer interactions per blade, with much sharper, higher amplitude acoustic signals. Moderate-amplitude BVI acoustic signals measured under the aft retreating quadrant of the rotor are shown to originate from the retreating side of the rotor.

17. Key Words (Suggested by Authors(s))	18. Distribution Statement
Rotor acoustics Blade-vortex interaction noise Acoustic directivity	Unclassified—Unlimited Subject Category 71

19. Security Classif.(of this report)	20. Security Classif.(of this page)	21. No. of Pages	22. Price
Unclassified	Unclassified	41	A03

For sale by the National Technical Information Service, Springfield, Virginia 22161-2171